Electronic Supplementary Material (ESI) for Physical Chemistry Chemical Physics.

Electronic Supplementary Information

Effects of self-hydrogen bonding among formamide molecules on the UCST-type liquid–liquid phase separation of binary solutions with imidazolium-based ionic liquid, [C$_n$mim][TFSI], studied by NMR, IR, MD simulations, and SANS

Masahiro Kawano[a], Atsuya Tashiro[a], Yuki Imamura[b], Moeno Yamada[b], Koichiro Sadakane[c], Hiroki Iwase[d], Masaru Matsugami[e], Bogdan A. Marekha[f], Abdenacer Idrissi[g], and Toshiyuki Takamuku[b,*]

[a] *Department of Chemistry and Applied Chemistry, Graduate School of Science and Engineering, Saga University, Honjo-machi, Saga 840-8502, Japan*

[b] *Department of Chemistry and Applied Chemistry, Faculty of Science and Engineering, Saga University, Honjo-machi, Saga 840-8502, Japan*

[c] *Faculty of Life and Medical Sciences, Doshisha University, 1-3 Tatara Miyakodani, Kyotanabe, Kyoto 610-0394, Japan*

[d] *Comprehensive Research Organization for Science and Society (CROSS), 162-1 Shirakata, Tokai, Ibaraki 319-1106, Japan*

[e] *Faculty of Liberal Arts, National Institute of Technology (KOSEN), Kumamoto College, 2659-2 Suya, Koshi, Kumamoto 861-1102, Japan*

[f] *Department of Biomolecular Mechanisms, Max Planck Institute for Medical Research, 29 Jahnstr., 69230 Heidelberg, Germany*

[g] *University of Lille, CNRS, UMR 8516 -LASIRe- Laboratoire Avancé de Spectroscopie pour les Interactions la Réactivité et l'environnement, F-5900 Lille, France*

*Corresponding Author
Toshiyuki Takamuku
E-mail: takamut@cc.saga-u.ac.jp

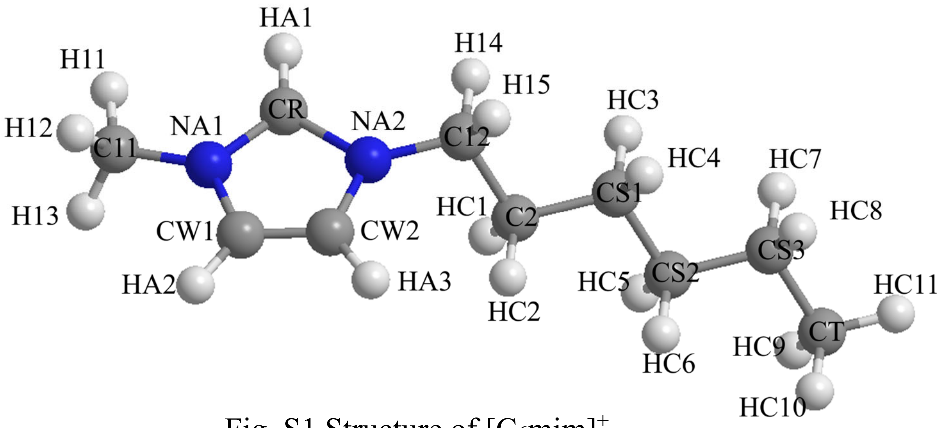

Fig. S1 Structure of $[C_6mim]^+$.

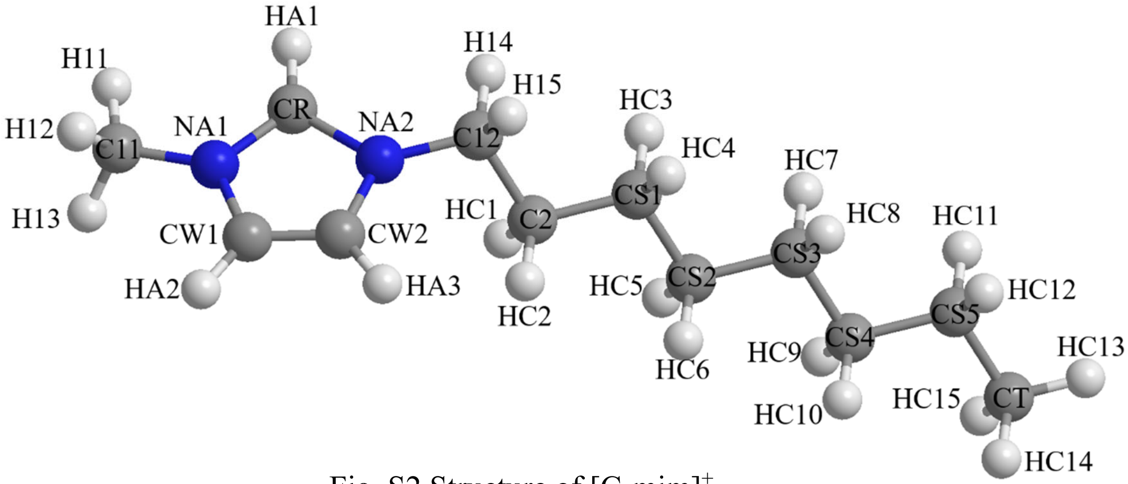

Fig. S2 Structure of $[C_8mim]^+$.

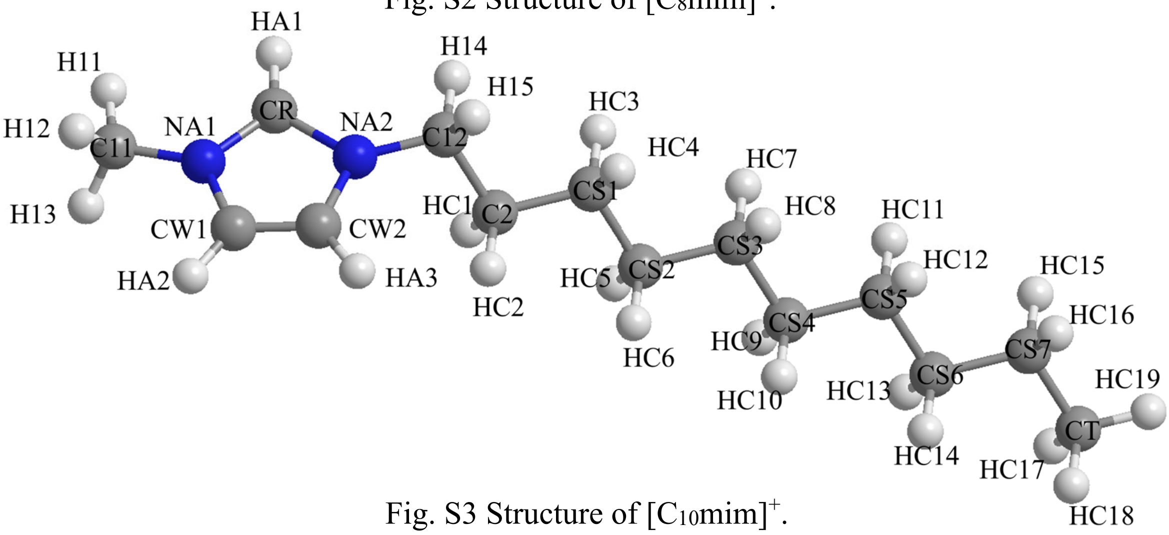

Fig. S3 Structure of $[C_{10}mim]^+$.

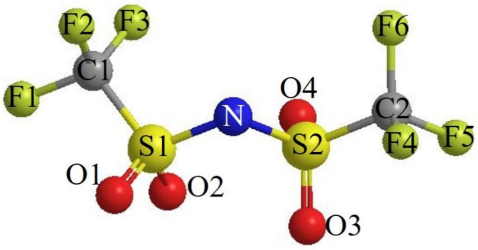

Fig. S4 Structure of $[TFSI]^-$.

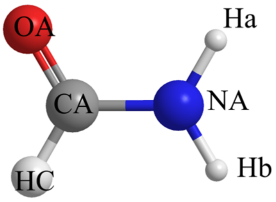

Fig. S5 Structure of FA.

Table S1 Atomic parameters for [C$_n$mim][TFSI] (n = 6, 8, and 10) and FA.

	Atom	Charge / e	σ / Å	ε / kcal mol^{-1}
[C$_n$mim]$^+$	NA*	0.150	3.250	0.170
	CR	-0.110	3.550	0.070
	HA*	0.210	2.420	0.030
	CW*	-0.130	3.550	0.070
	C1*	-0.170	3.500	0.066
	H1*	0.130	2.500	0.030
	C2	0.010	3.500	0.066
	HC*	0.060	2.500	0.030
	CS*	-0.120	3.500	0.066
	CT	-0.180	3.500	0.066
[TFSI]$^-$	N	-0.660	3.250	0.170
	S*	1.020	3.550	0.250
	C*	0.350	3.500	0.066
	O*	-0.530	2.960	0.210
	F*	-0.160	2.950	0.053
FA	CA	0.140	3.806	0.074
	HC	0.175	2.456	0.011
	NA	-0.416	3.299	0.119
	Ha	0.317	0.000	0.000
	Hb	0.312	0.000	0.000
	OA	-0.528	3.004	0.147

X* means chemically equivalent X atoms in [C$_n$mim]$^+$ and [TFSI]$^-$ as depicted in Fig. S1–S4.

Table S2 Bond stretching parameters for [C$_n$mim][TFSI] (n = 6, 8, and 10) and FA.

	Bond	r / Å	k / kcal mol^{-1}
[C$_n$mim]$^+$	CR-NA*	1.315	477.0
	C1*-H1*	1.090	
	NA*-C1*	1.466	337.0
	CR-HA*	1.080	
	CW*-NA*	1.378	427.0
	CW*-CW*	1.341	520.0
	CW1-HA*	1.080	
	C1*-C2	1.529	268.0
	C2-HC*	1.090	
	C2-CS*	1.529	268.0
	CS1-HC*	1.090	
	CS*-CS*	1.529	268.0
	CS*-CT	1.529	268.0
	CT-HC*	1.090	
[TFSI]$^-$	N-S*	1.570	374.7
	S*-C*	1.818	232.9
	S*-O*	1.437	636.8

	C*-F*	1.323	441.7
FA	CA-NA	1.333	268.0
	CA-OA	1.229	340.0
	CA-HC	1.098	
	NA-Ha	1.012	
	NA-Hb	1.012	

X* means chemically equivalent X atoms in $[C_n\text{mim}]^+$ and $[\text{TFSI}]^-$ as depicted in Fig. S1–S4.

Table S3 Angle bending parameters for $[C_n\text{mim}][\text{TFSI}]$ (n = 6, 8, and 10) and FA.

	Angle	K / kcal mol^{-1} degree^{-2}	θ / degree
$[C_n\text{mim}]^+$	H1*-C1*-H1*	33.00	107.8
	H1*-C1*-NA*	37.50	110.7
	C1*-NA*-CR	70.00	126.4
	C1*-NA*-CW*	70.00	125.6
	NA*-CR-HA*	35.00	125.1
	NA*-CR-NA*	70.00	109.8
	CR-NA*-CW*	70.00	108.0
	NA*-CW*-CW*	70.00	107.1
	NA*-CW*-HA*	35.00	122.0
	HA*-CW*-CW*	35.00	130.9
	NA*-C1*-C2	58.30	112.7
	H1*-C1*-C2	37.50	110.7
	C1*-C2-HC*	37.50	110.7
	C1*-C2-CS*	58.30	112.7
	HC*-C2-CS*	37.50	110.7
	HC*-CS*-C2	37.50	110.7
	HC*-CS*-CS*	37.50	110.7
	HC*-CS*-CT	37.50	110.7
	HC*-CT-CS*	37.50	110.7
	HC*-CT-HC*	33.00	107.8
	HC*-C2-HC*	33.00	107.8
	HC*-CS*-HC*	33.00	107.8
	C2-CS*-CS*	58.30	112.7
	CS*-CS*-CS*	58.30	112.7
	CS*-CS*-CT	58.30	112.7
$[\text{TFSI}]^-$	N-S*-C*	91.30	103.5
	N-S*-O*	94.20	113.6
	S*-N-S*	80.10	125.6
	S*-C*-F*	82.90	111.7
	C*-S*-O*	103.90	102.6
	O*-S*-O*	115.70	118.5
	F*-C*-F*	93.30	107.1
FA	OA-CA-NA	80.00	124.6
	HC-CA-NA	40.00	113.8
	CA-NA-Ha	35.00	119.1

CA-NA-Hb	35.00	119.1
HC-CA-OA	35.00	120.4
Hb-NA-Ha	35.00	120.6

X* means chemically equivalent X atoms in [C$_n$mim]$^+$ and [TFSI]$^-$ as depicted in Fig. S1–S4.

Table S4 Dihedral parameters for [C$_n$mim][TFSI] (n = 6, 8, and 10) and FA.

	Dihedral	V_1 / kcal mol^{-1}	V_2 / kcal mol^{-1}	V_3 / kcal mol^{-1}	V_4/ kcal mol^{-1}
[C$_n$mim]$^+$	CR-NA*-C1*-H1*	0.000	0.000	0.000	0.000
	CW*-NA*-C1*-H1*	0.000	0.000	0.124	0.000
	C1*-NA*-CR-HA*	0.000	4.650	0.000	0.000
	NA*-CR-NA*-C1*	0.000	4.650	0.000	0.000
	CW*-CW*-NA-C1*	0.000	3.000	0.000	0.000
	C1*-NA*-CW*-HA*	0.000	3.000	0.000	0.000
	NA*-CW*-CW*-HA*	0.000	10.750	0.000	0.000
	NA*-CW*-CW*-NA*	0.000	10.750	0.000	0.000
	CW*-NA*-CR-HA*	0.000	4.650	0.000	0.000
	CR-NA*-CW*-HA*	0.000	3.000	0.000	0.000
	CR-NA*-CW*-CW*	0.000	3.000	0.000	0.000
	C1*-C2-CS*-HC*	0.000	0.000	0.366	0.000
	HC*-C2-CS*-HC*	0.000	0.000	0.318	0.000
	HC*-CS*-CS*-HC*	0.000	0.000	0.318	0.000
	HC*-CS*-CT-HC*	0.000	0.000	0.318	0.000
	HC*-CS*-CS*-CT	0.000	0.000	0.366	0.000
	C1*-C2-CS*-CS*	1.739	-0.157	0.279	0.000
	C2-CS*-CS*-CS*	1.739	-0.157	0.279	0.000
	CS*-CS*-CS*-CS*	1.739	-0.157	0.279	0.000
	CS*-CS*-CS*-CT	1.739	-0.157	0.279	0.000
	CS*-CS*-CS*-HC*	0.000	0.000	0.366	0.000
	C2-CS*-CS*-HC*	0.000	0.000	0.366	0.000
	CS*-CS*-C2-HC*	0.000	0.000	0.366	0.000
	CS*-CS*-CT-HC*	0.000	0.000	0.366	0.000
	HA*-CW*-CW*-HA*	0.000	10.750	0.000	0.000
	CW*-NA*-C1*-C2	-1.709	1.459	0.190	0.000
	CR-NA*-C1*-C2	-1.259	0.000	0.000	0.000
	NA*-C1*-C2-CS*	-1.787	0.756	-0.287	0.000
	H1*-C1*-C2-HC*	0.000	0.000	0.318	0.000
	NA*-C1*-C2-HC*	0.000	0.000	0.088	0.000
	CS*-C2-C1*-H1*	0.000	0.000	0.366	0.000
	NA*-CR-NA*-CW*	0.000	4.650	0.000	0.000
[TFSI]$^-$	N-S*-C*-F*	0.000	0.000	0.316	0.000
	S*-N-S*-C*	7.829	-2.489	-0.763	0.000
	S*-N-S*-O*	0.000	0.000	-0.003	0.000
	O*-S*-C*-F*	0.000	0.000	0.347	0.000
FA	OA-CA-NA-Ha	0.000	4.900	0.450	0.000
	OA-CA-NA-Hb	0.000	4.900	0.450	0.000
	HC-CA-NA-Ha	0.000	4.900	0.450	0.000

HC-CA-NA-Hb	0.000	4.900	0.450	0.000

X* means chemically equivalent X atoms in [C$_n$mim]$^+$ and [TFSI]$^-$ as depicted in Fig. S1–S4.

Table S5 Densities of d_{MD} derived from MD simulations and d_{exp} experimentally determined, and the deviation of Δd, respectively.

[C$_6$mim][TFSI]–FA system					[C$_8$mim][TFSI]–FA system				
x_{FA}	T / K	d_{MD} / g cm^{-3}	d_{exp} / g cm^{-3}	Δd / %	x_{FA}	T / K	d_{MD} / g cm^{-3}	d_{exp} / g cm^{-3}	Δd / %
0	348.2	1.303	1.327*	-1.8	0	373.2	1.241	1.255*	-1.1
	318.2	1.320	1.354	-2.5		343.2	1.259	1.281*	-1.8
	298.2	1.331	1.372	-3.0		323.2	1.270	1.299	-2.2
	278.2	1.343	1.390*	-3.4		293.2	1.283	1.316	-2.5
	248.2	1.360				273.2	1.301	1.343*	-3.1
0.881	348.2	1.222	1.207*	1.3	0.900	373.2	1.167	1.154*	1.2
	318.2	1.250	1.234	1.2		343.2	1.194	1.181*	1.1
	308.2	1.258	1.244	1.2		333.2	1.203	1.190	1.1
	298.2	1.268	1.253	1.2		323.2	1.212	1.199	1.1
	288.2	1.277	1.262	1.2		313.2	1.221	1.208*	1.0
	278.2	1.286	1.272*	1.2		303.2	1.229	1.217*	1.0
	248.2	1.310				273.2	1.257	1.244*	1.0
[C$_{10}$mim][TFSI]–FA system					[C$_{10}$mim][TFSI]–FA system				
x_{FA}	T / K	d_{MD} / g cm^{-3}	d_{exp} / g cm^{-3}	Δd / %	x_{FA}	T / K	d_{MD} / g cm^{-3}	d_{exp} / g cm^{-3}	Δd / %
0	398.2	1.184	1.194*	-0.85	0.926	348.2	1.158		
	368.2	1.203	1.219*	-1.3		338.2	1.167		
	348.2	1.216	1.236*	-1.6		328.2	1.175		
	328.2	1.229	1.253	-2.0		298.2	1.202		
	298.2	1.247	1.279	-2.5	1	398.2	1.042	1.045*	-0.32
0.926	398.2	1.113				348.2	1.083	1.087*	-0.38
	368.2	1.140				298.2	1.122	1.129	-0.62
	358.2	1.149				248.2	1.160		

* The values were estimated by extrapolation for densities measured.

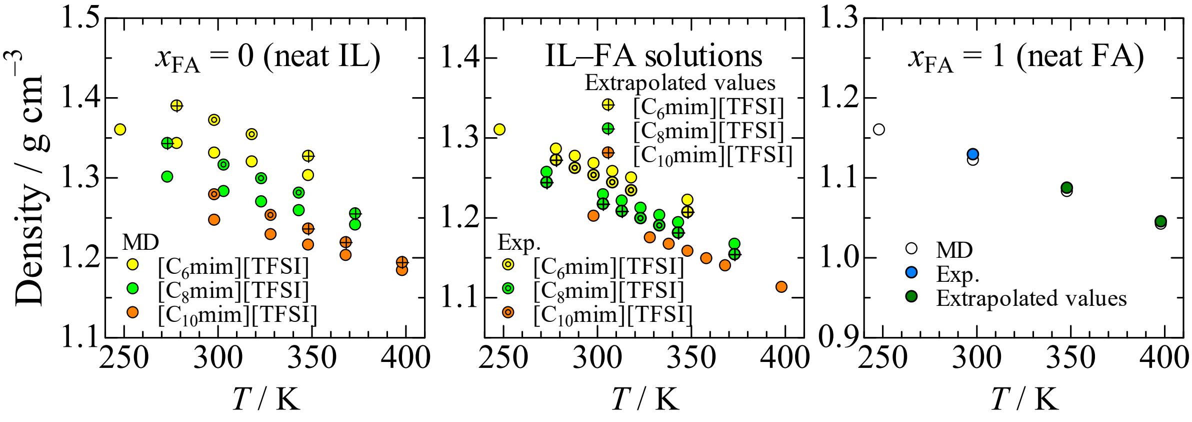

Fig. S6 Simulated and experimental densities for [C$_n$mim][TFSI]–FA system at x_{FA} = 0 (neat IL) (left), UCST x_{FA} = 0.881 (n = 6), 0.900 (n = 8), and 0.926 (n = 10) (middle), and x_{FA} = 1 (neat FA) (right), as a function of temperature.

Table S6 Phase separation points in the liquid–liquid phase diagrams of [C$_n$mim][TFSI]–FA and –FA-d_2 systems (Fig. 2 and S27, respectively).

n = 6		n = 8		n = 10		n = 12		n = 6 (FA-d_2)	
x_{FA}	T / K	x_{FA}	T / K	x_{FA}	T / K	x_{FA}	T / K	$x_{FA\text{-}d2}$	T / K
0.6043	279.0	0.4950	280.8	0.5063	300.4	0.4138	296.0	0.8005	294.2
0.7063	289.3	0.6130	298.2	0.6110	314.2	0.4992	312.3	0.8400	296.8
0.7488	292.8	0.7048	305.9	0.7016	330.3	0.5901	330.5	0.8810	295.7
0.8029	295.9	0.7532	314.3	0.7505	334.1	0.6487	338.1	0.9200	297.2
0.8511	297.2	0.7998	318.2	0.8033	343.3	0.7042	350.4	0.9500	290.1
0.8698	297.2	0.8188	319.3	0.8499	273.2	0.7517	360.0		
0.8812	297.3	0.8497	321.0	0.8694	345.7	0.9702	363.0	n = 8 (FA-d_2)	
0.8902	297.3	0.8703	322.0	0.8905	346.0	0.9800	359.0	$x_{FA\text{-}d2}$	T / K
0.8999	297.2	0.8995	322.1	0.9003	346.7	0.9898	338.8	0.8300	319.7
0.9125	297.2	0.9497	320.6	0.9209	346.9			0.8764	322.0
0.9199	297.2	0.9698	313.5	0.9256	346.9			0.9002	322.1
0.9301	296.6			0.9303	346.9			0.9301	321.1
0.9495	292.8			0.9500	345.7				
0.9702	279.4			0.9770	335.0				
				0.9900	303.6				

S3.2 ^{1}H NMR peaks for the two amino H atoms of FA

Fig. S13, S15, S17, and S19 display ^{1}H NMR spectra of neat FA and the [C$_n$mim][TFSI]–FA solutions with n = 6, 8, and 10, respectively, as a function of temperature. At the lower temperatures below ~338.2 K, two peaks for the amino H atoms separately appear around 8 ppm because the exchange rate of the two H atoms decreases with lowering temperature. The two peaks at the low and high magnetic fields can be assigned to the cis Ha and trans Hb atoms against the formyl O atom, respectively (see the notation of FA H atoms in Fig. 1 in the main text). However, the two peaks overlap as one broader peak at the higher temperatures above ~338.2 K. In Fig. 9 of the main text, the values above 338.2 K correspond to the shifts for the peak where the signals of the Ha and Hb atoms overlap with each other.

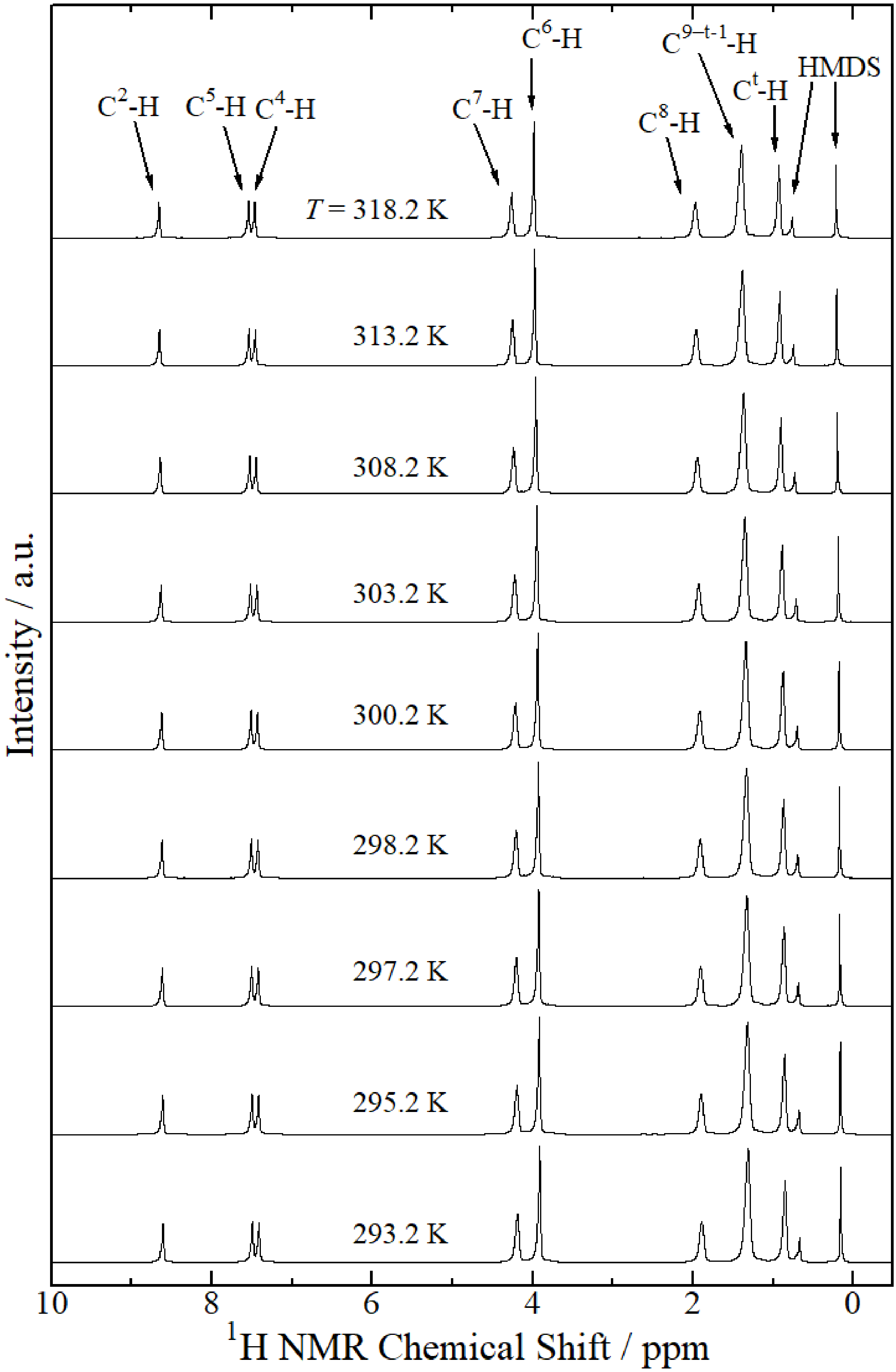

Fig. S7 ^{1}H NMR spectra of [C$_6$mim][TFSI]–FA system at x_{FA} = 0 (neat IL) as a function of temperature from 318.2 to 293.2 K.

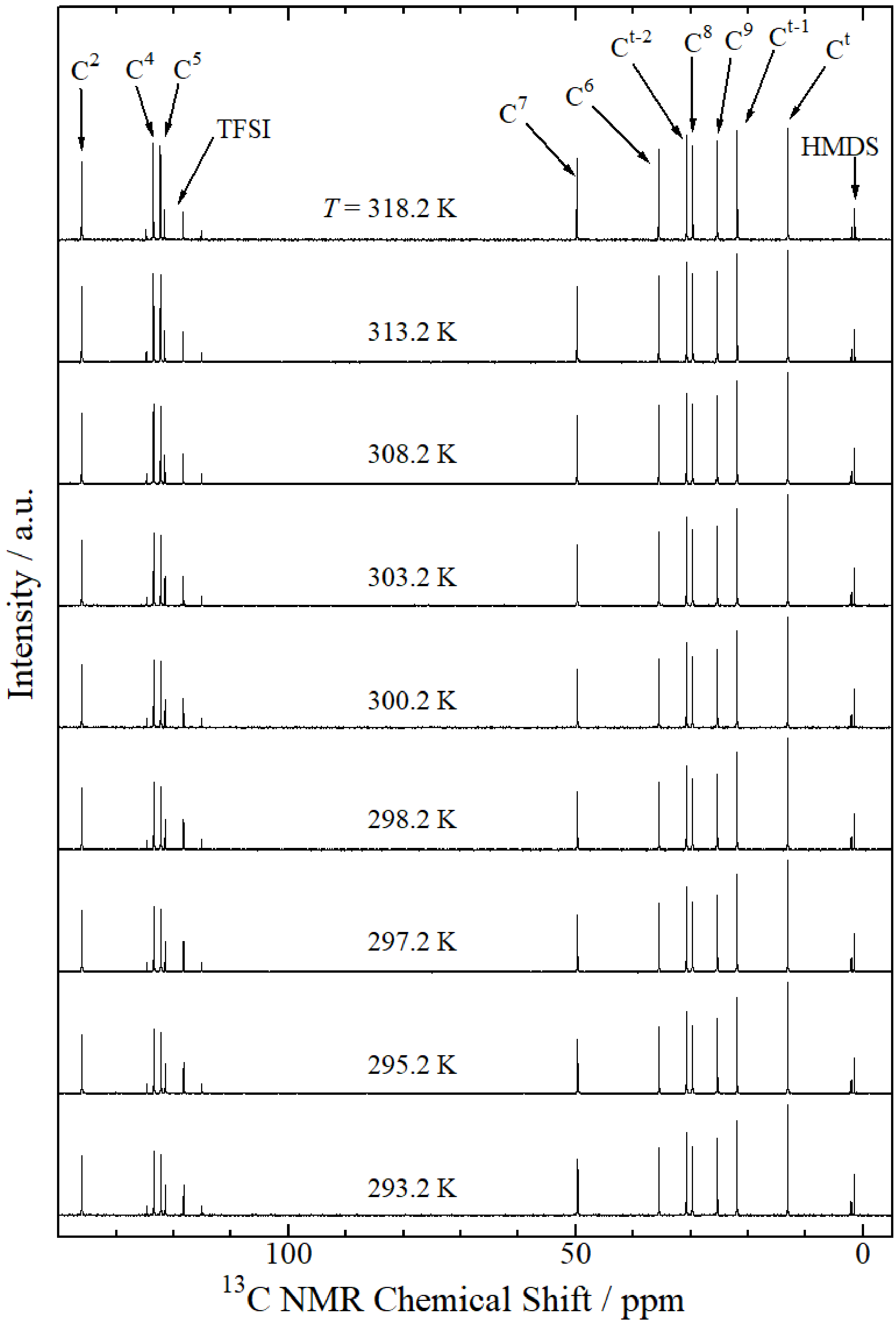

Fig. S8 ^{13}C NMR spectra of [C_6mim][TFSI]–FA system at x_{FA} = 0 (neat IL) as a function of temperature from 318.2 to 293.2 K.

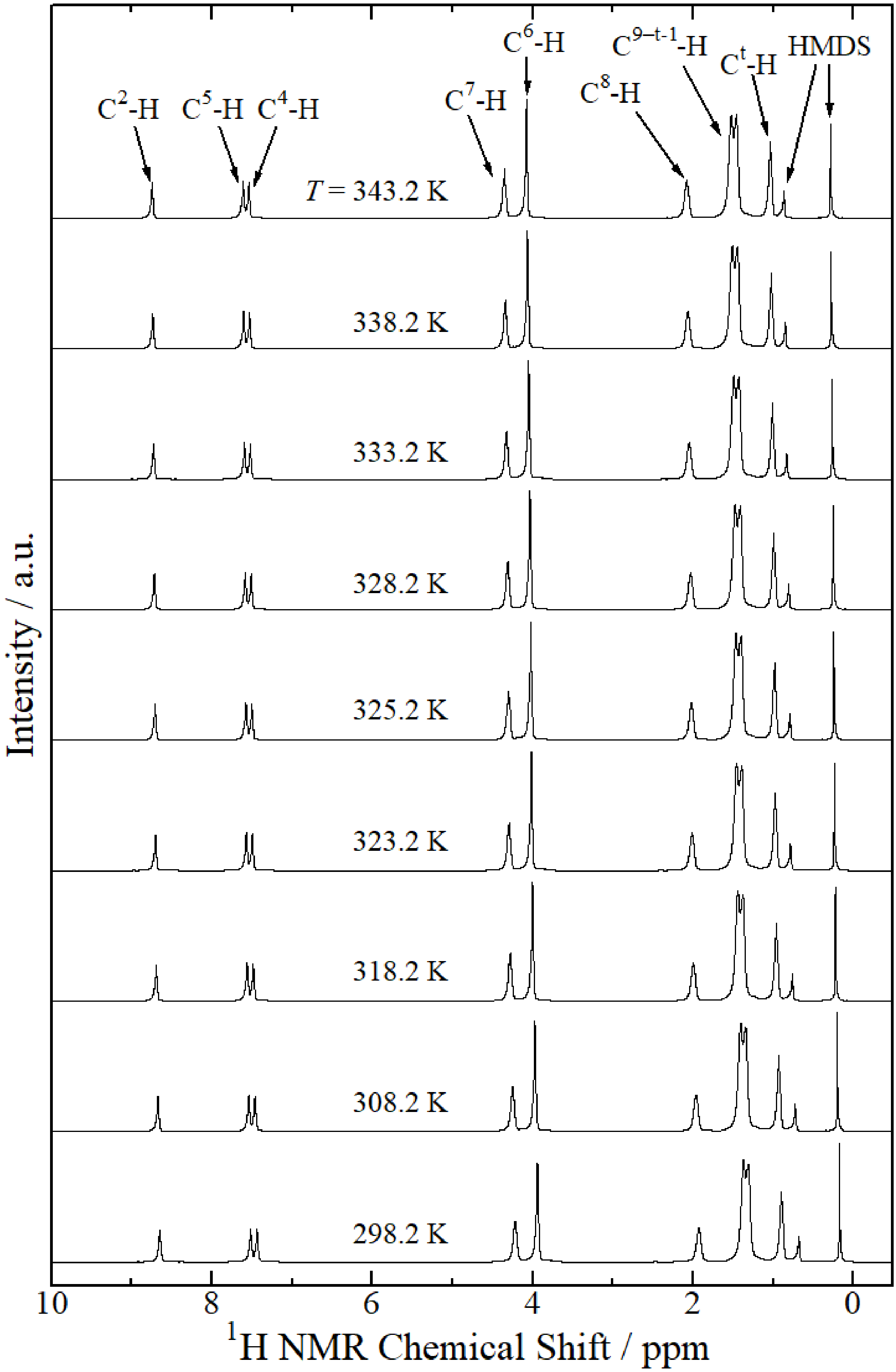

Fig. S9 ^{1}H NMR spectra of [C$_8$mim][TFSI]–FA system at x_{FA} = 0 (neat IL) as a function of temperature from 343.2 to 298.2 K.

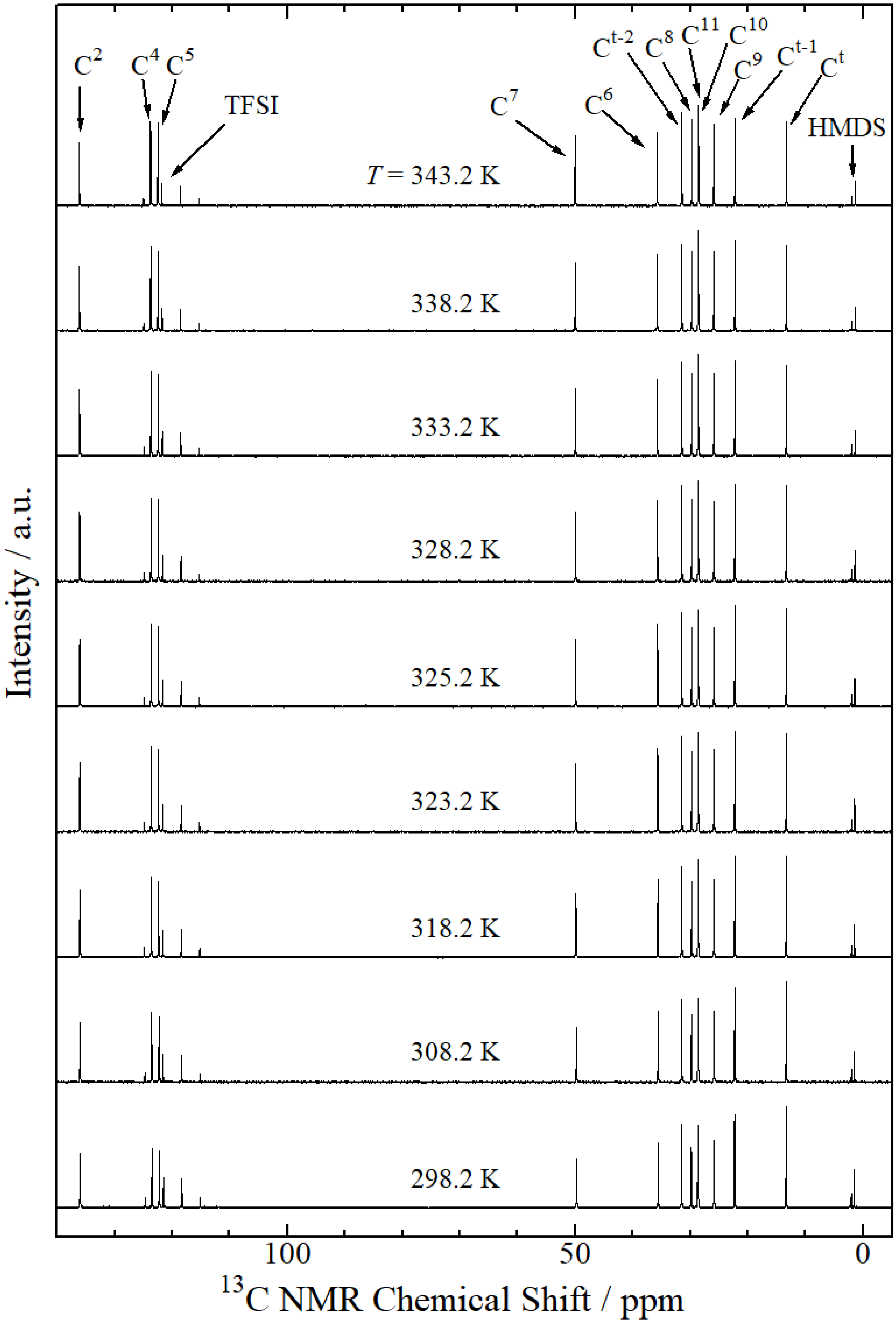

Fig. S10 ^{13}C NMR spectra of [C$_8$mim][TFSI]–FA system at $x_{FA} = 0$ (neat IL) as a function of temperature from 343.2 to 298.2 K.

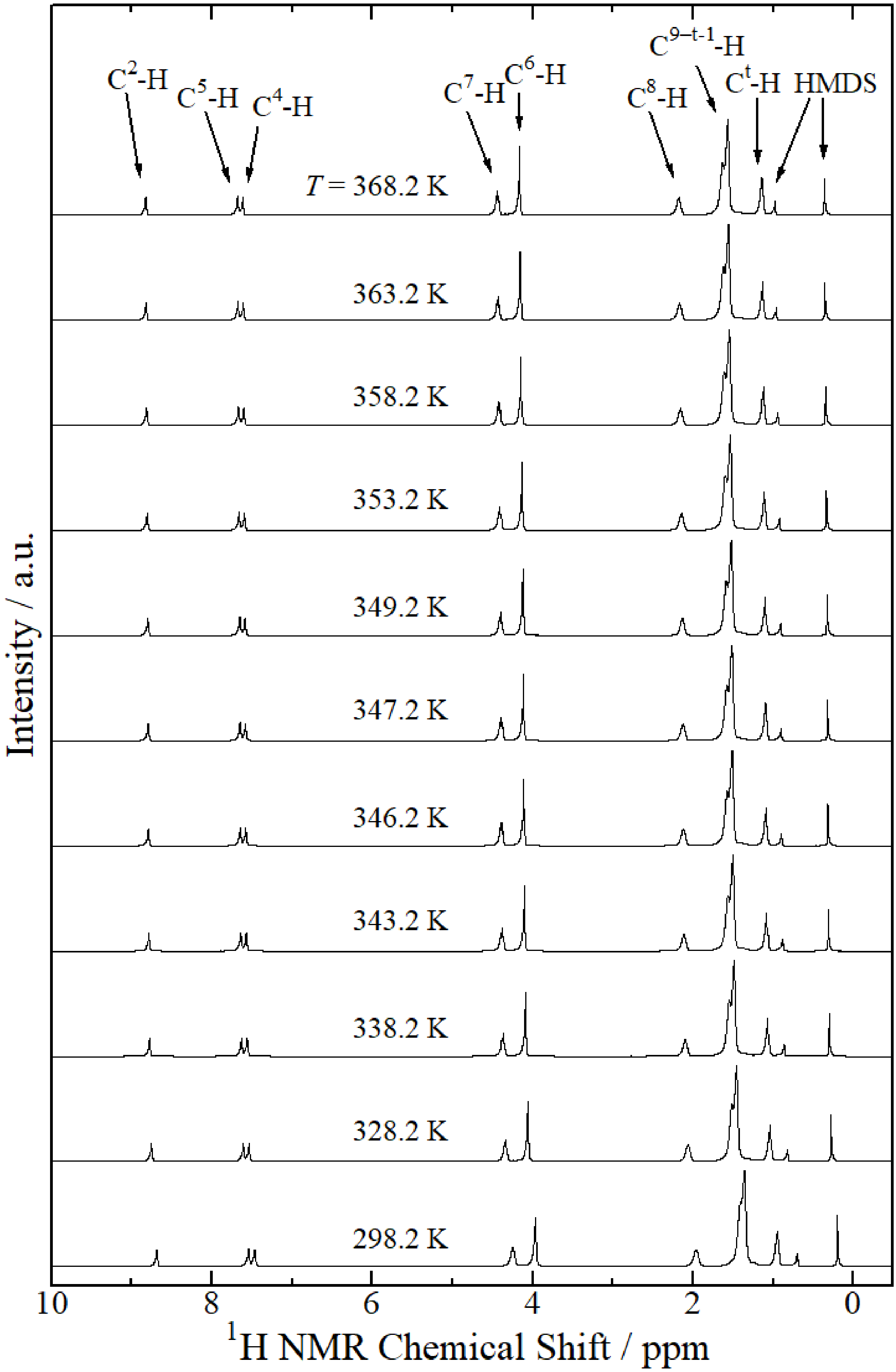

Fig. S11 ^{1}H NMR spectra of [C_{10}mim][TFSI]–FA system at x_{FA} = 0 (neat IL) as a function of temperature from 368.2 to 298.2 K.

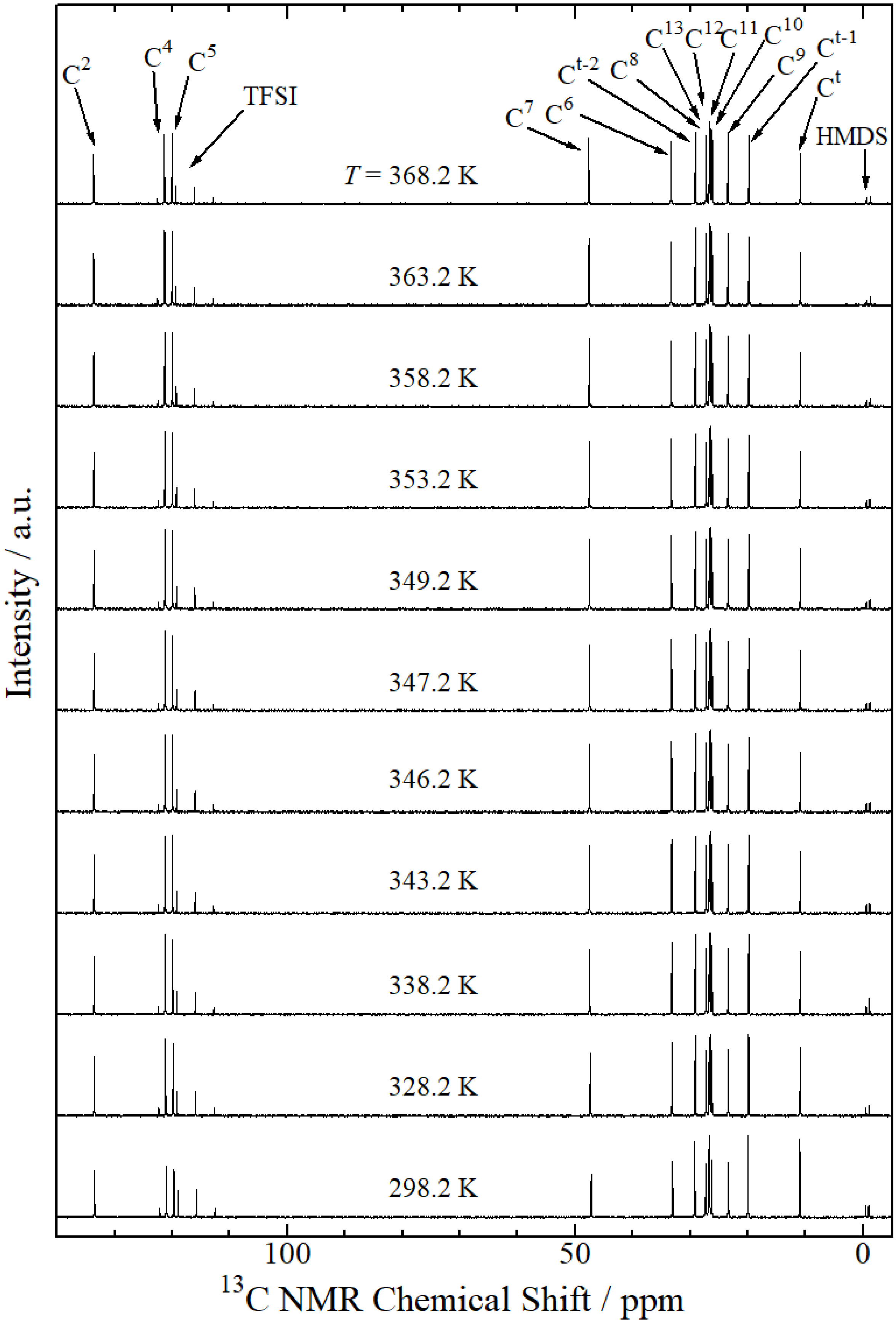

Fig. S12 ^{13}C NMR spectra of [C$_{10}$mim][TFSI]–FA system at x_{FA} = 0 (neat IL) as a function of temperature from 368.2 to 298.2 K.

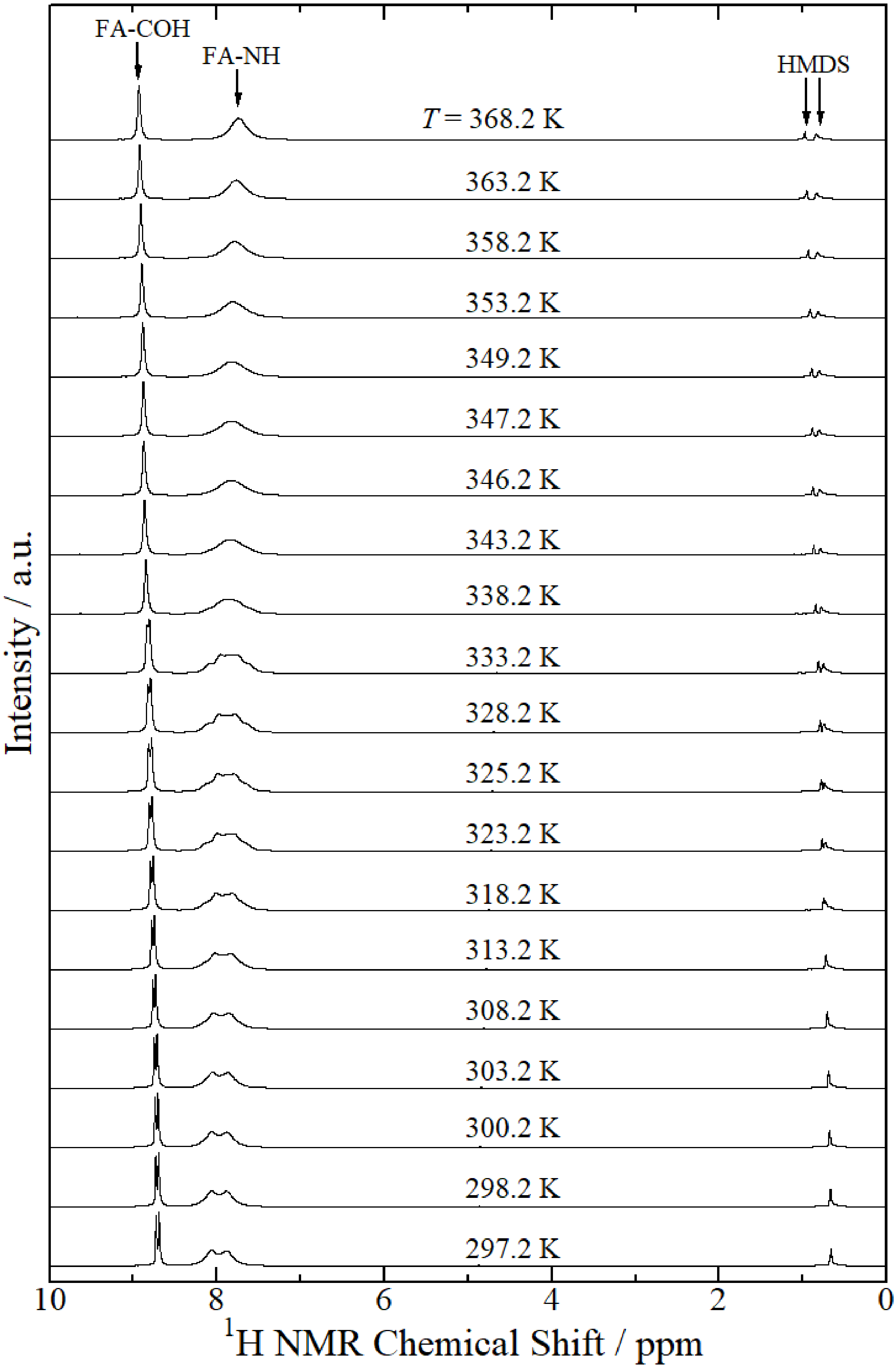

Fig. S13 ^{1}H NMR spectra of neat FA as a function of temperature from 368.2 to 297.2 K.

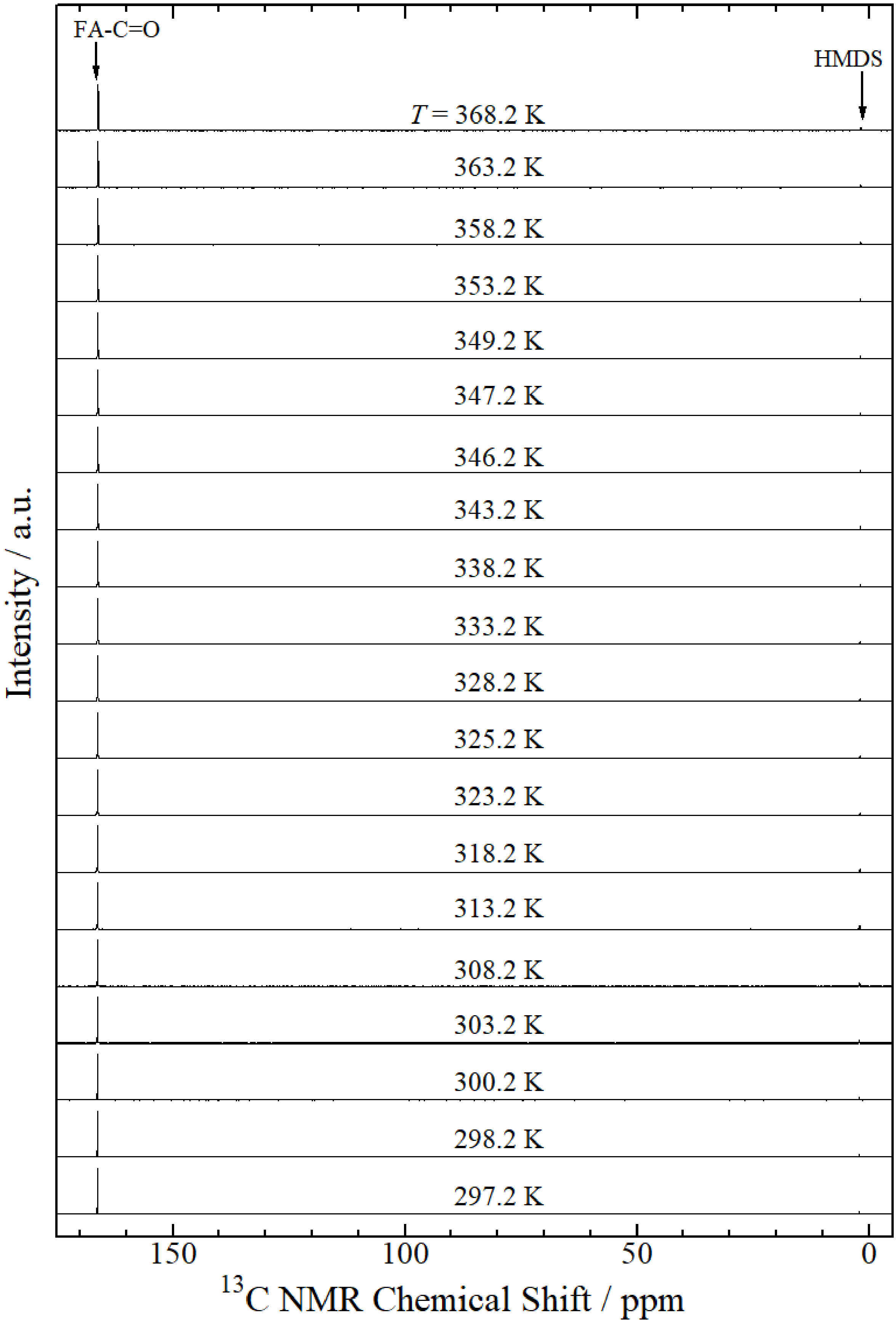

Fig. S14 ^{13}C NMR spectra of neat FA as a function of temperature from 368.2 to 297.2 K.

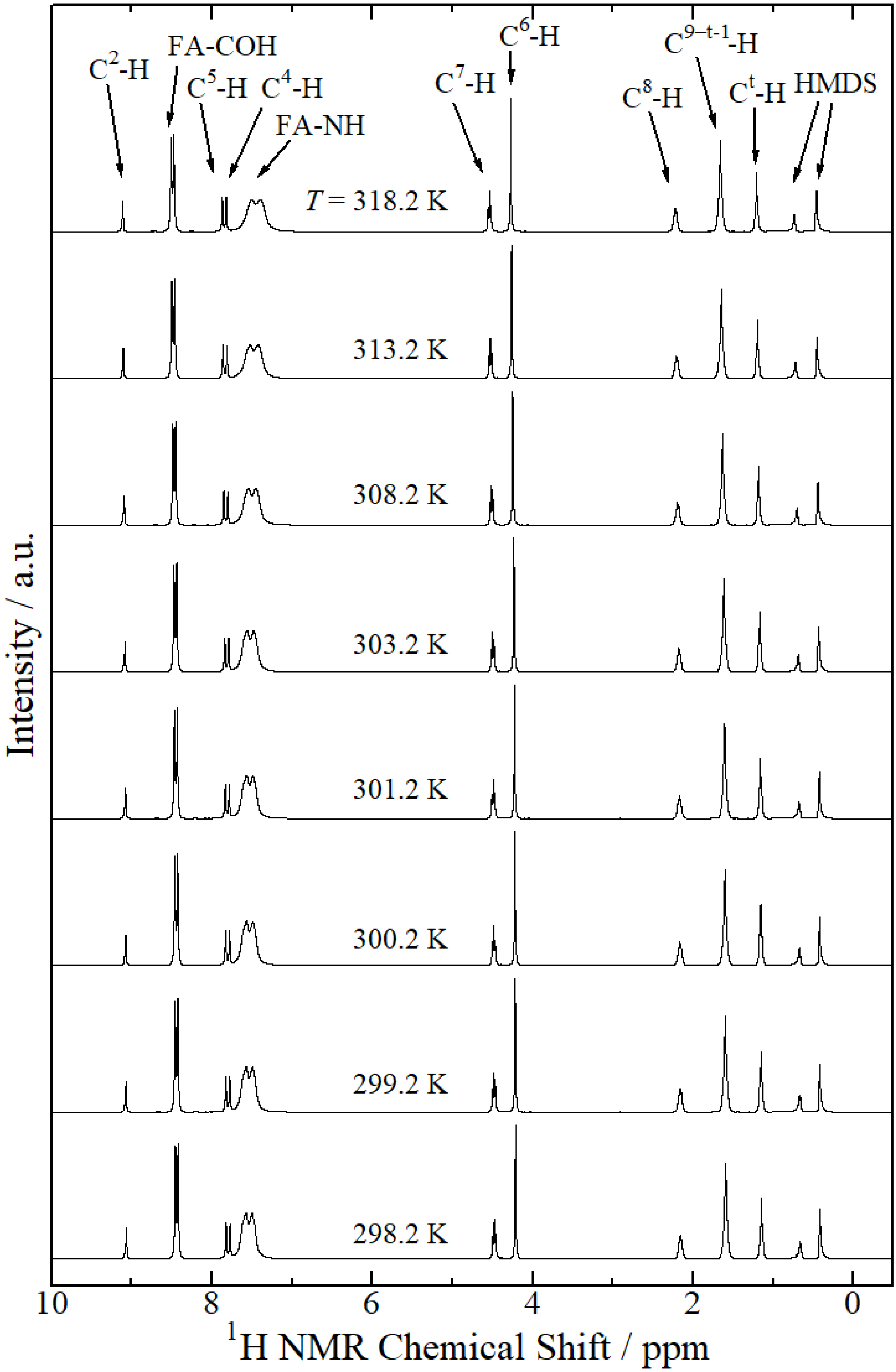

Fig. S15 ^{1}H NMR spectra of [C$_6$mim][TFSI]–FA system at x_{FA} = 0.881 as a function of temperature from 318.2 to 298.2K.

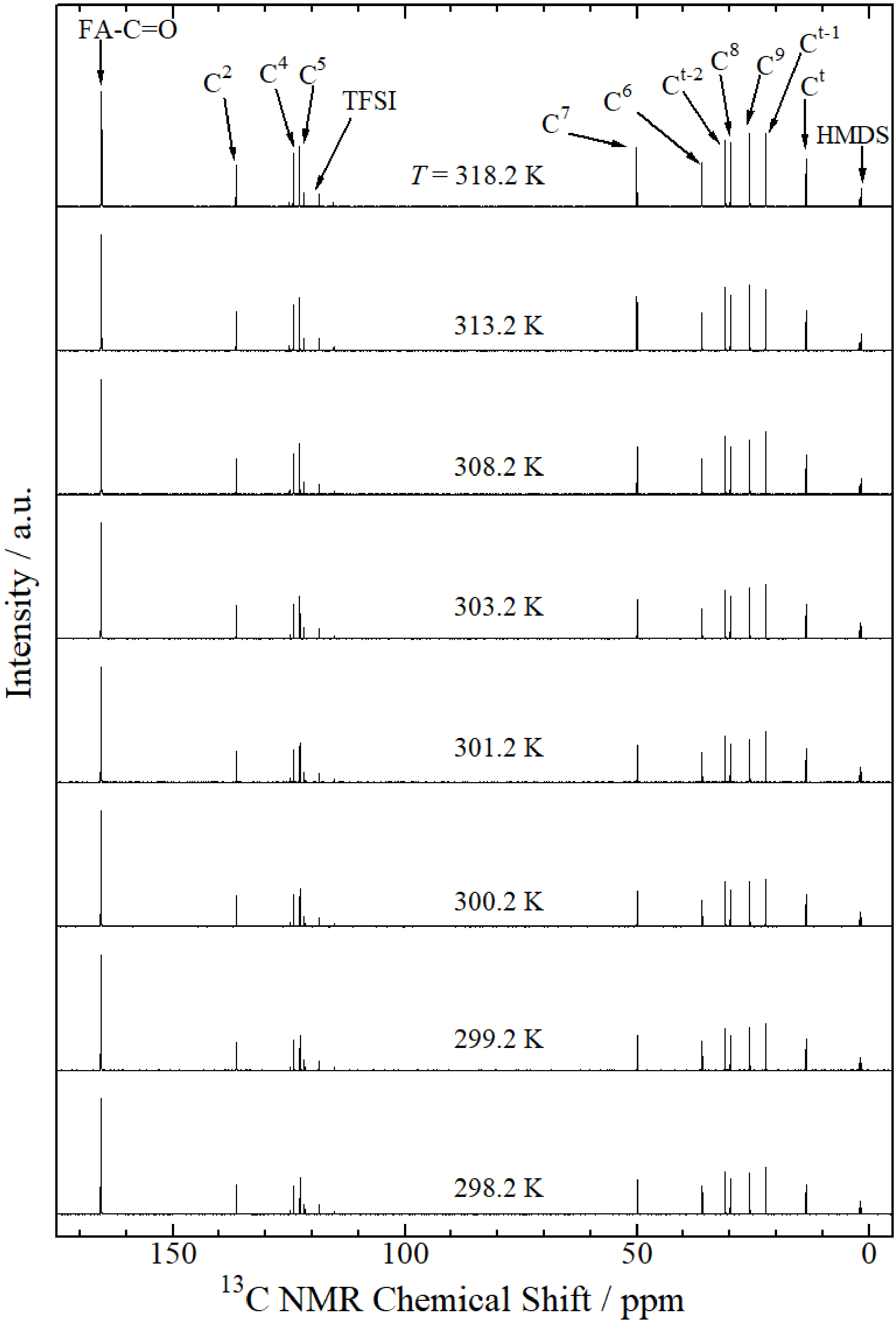

Fig. S16 ^{13}C NMR spectra of [C$_6$mim][TFSI]–FA system at x_{FA} = 0.881 as a function of temperature from 318.2 to 298.2 K.

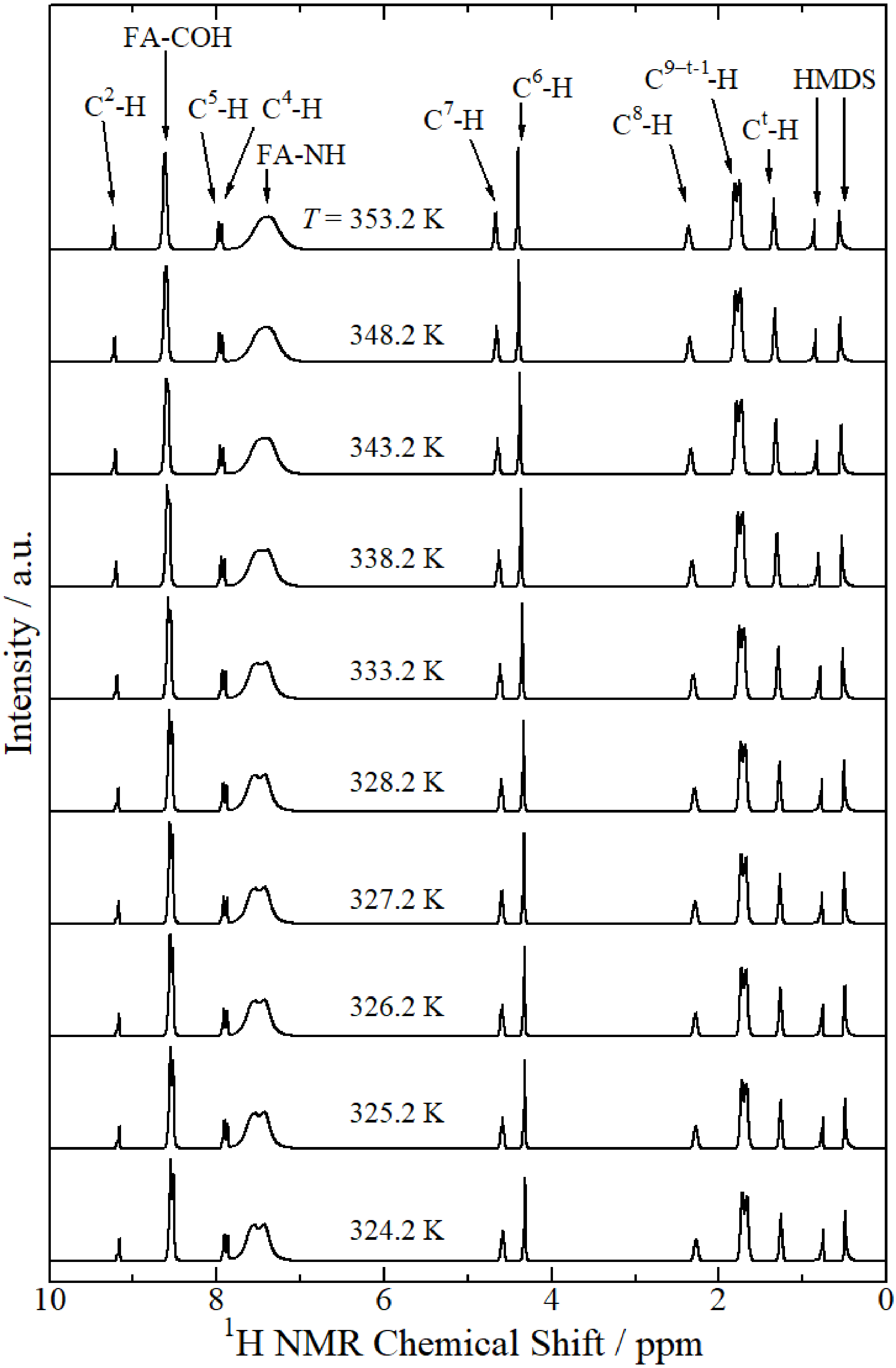

Fig. S17 ^{1}H NMR spectra of [C$_8$mim][TFSI]–FA system at x_{FA} = 0.900 as a function of temperature from 353.2 to 324.2 K.

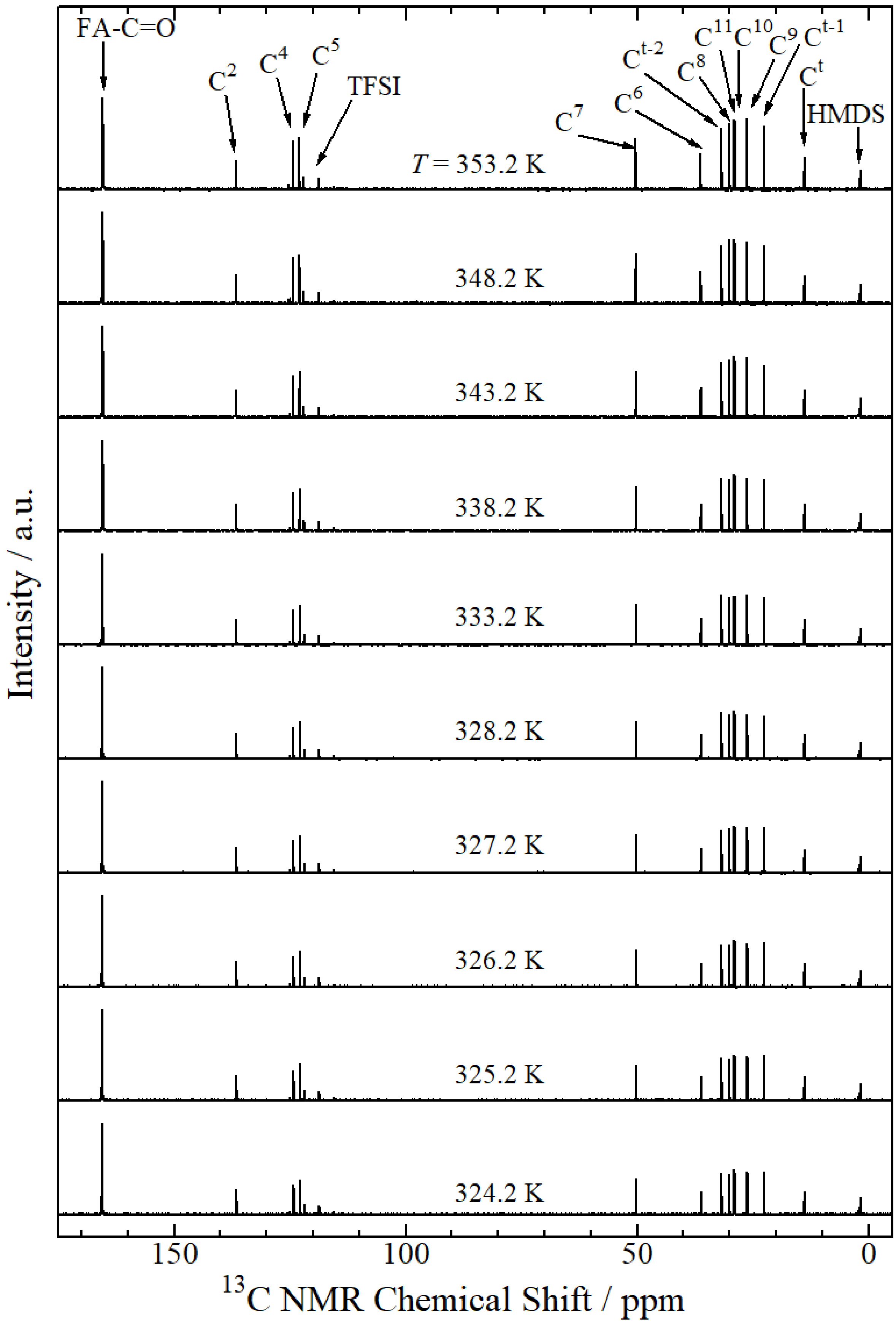

Fig. S18 ^{13}C NMR spectra of [C$_8$mim][TFSI]–FA system at x_{FA} = 0.900 as a function of temperature from 353.2 to 324.2 K.

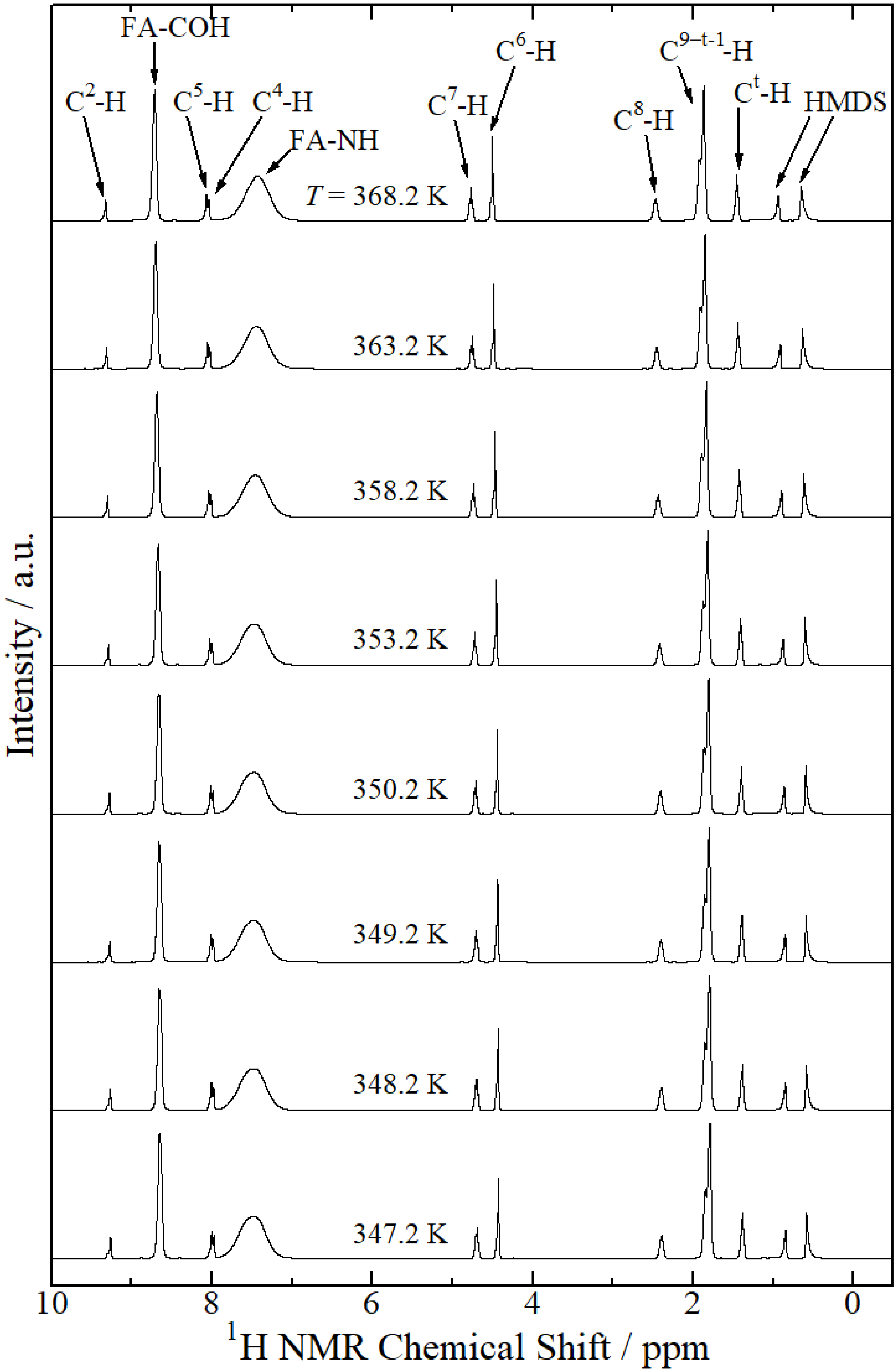

Fig. S19 ^{1}H NMR spectra of [C$_{10}$mim][TFSI]–FA system at x_{FA} = 0.926 as a function of temperature from 368.2 to 347.2 K.

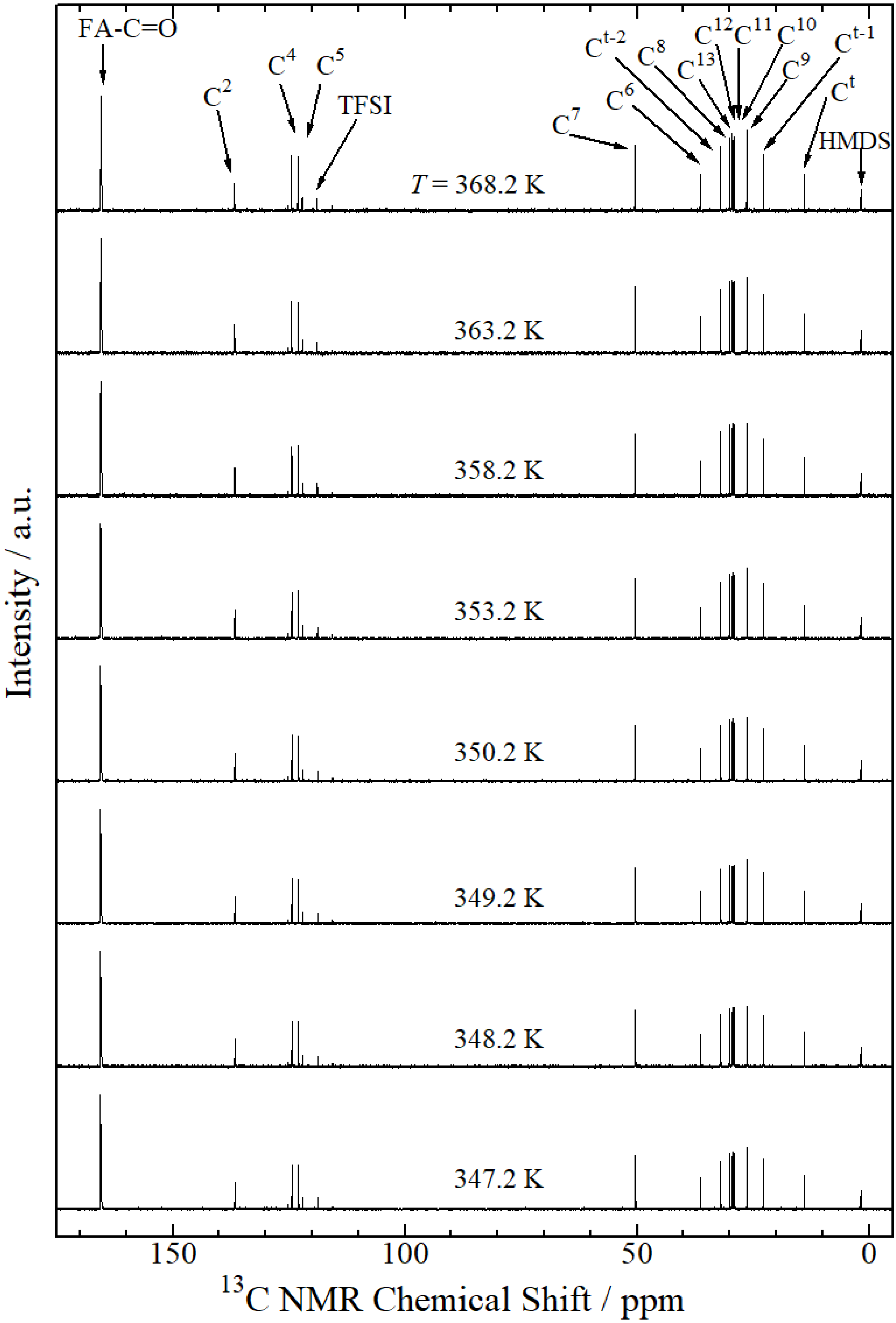

Fig. S20 ^{13}C NMR spectra of [C_{10}mim][TFSI]–FA system at x_{FA} = 0.926 as a function of temperature from 368.2 to 347.2 K.

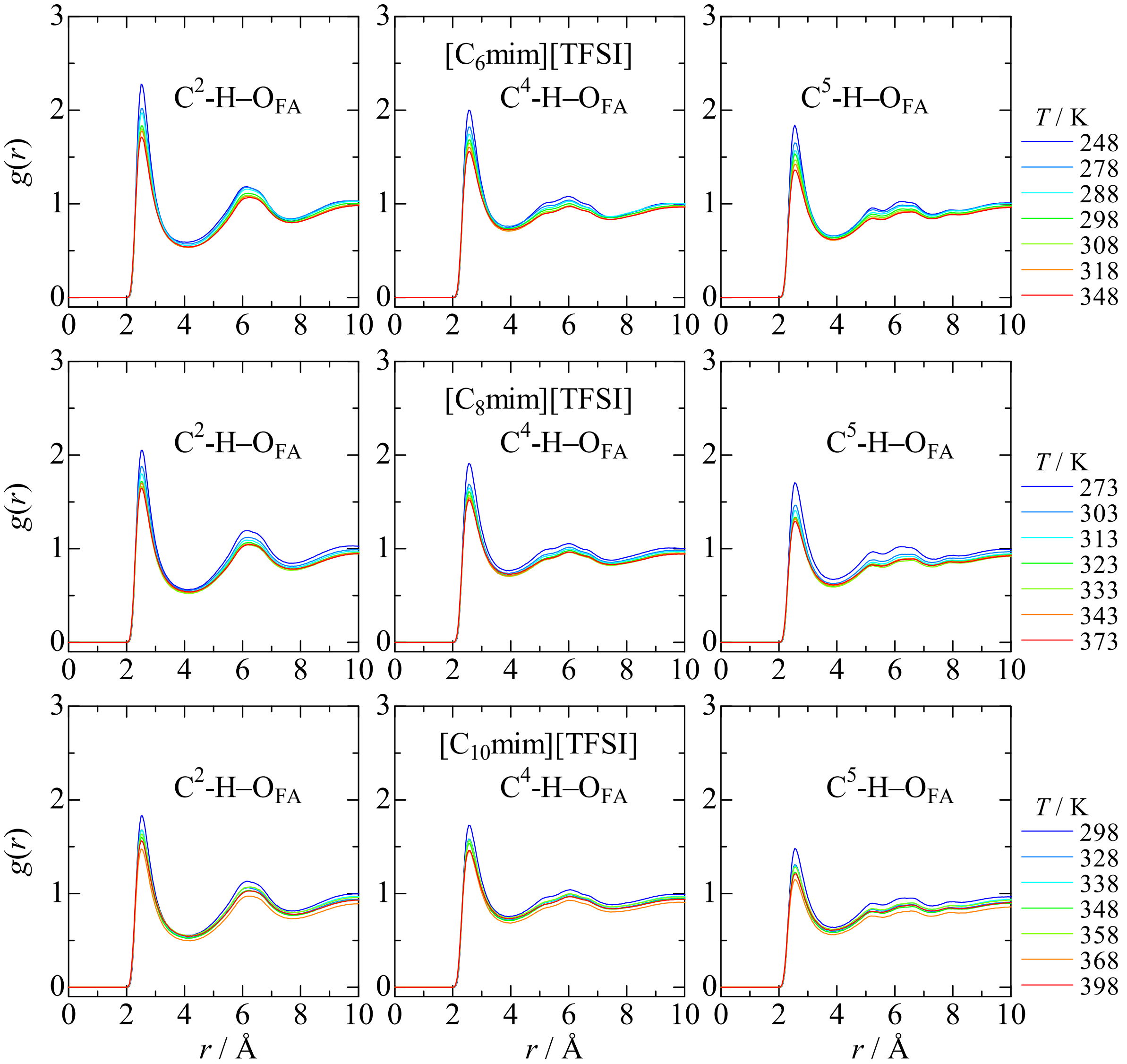

Fig. S21 Temperature dependence of MD pair correlation functions, $g(r)$s, for the $C^{2,4,5}$-H–O_{FA} interactions in $[C_n mim][TFSI]$–FA solutions (top: n = 6, middle: n = 8, and bottom n = 10, respectively) at each UCST composition (x_{FA} = 0.881, 0.900, and 0.926, respectively).

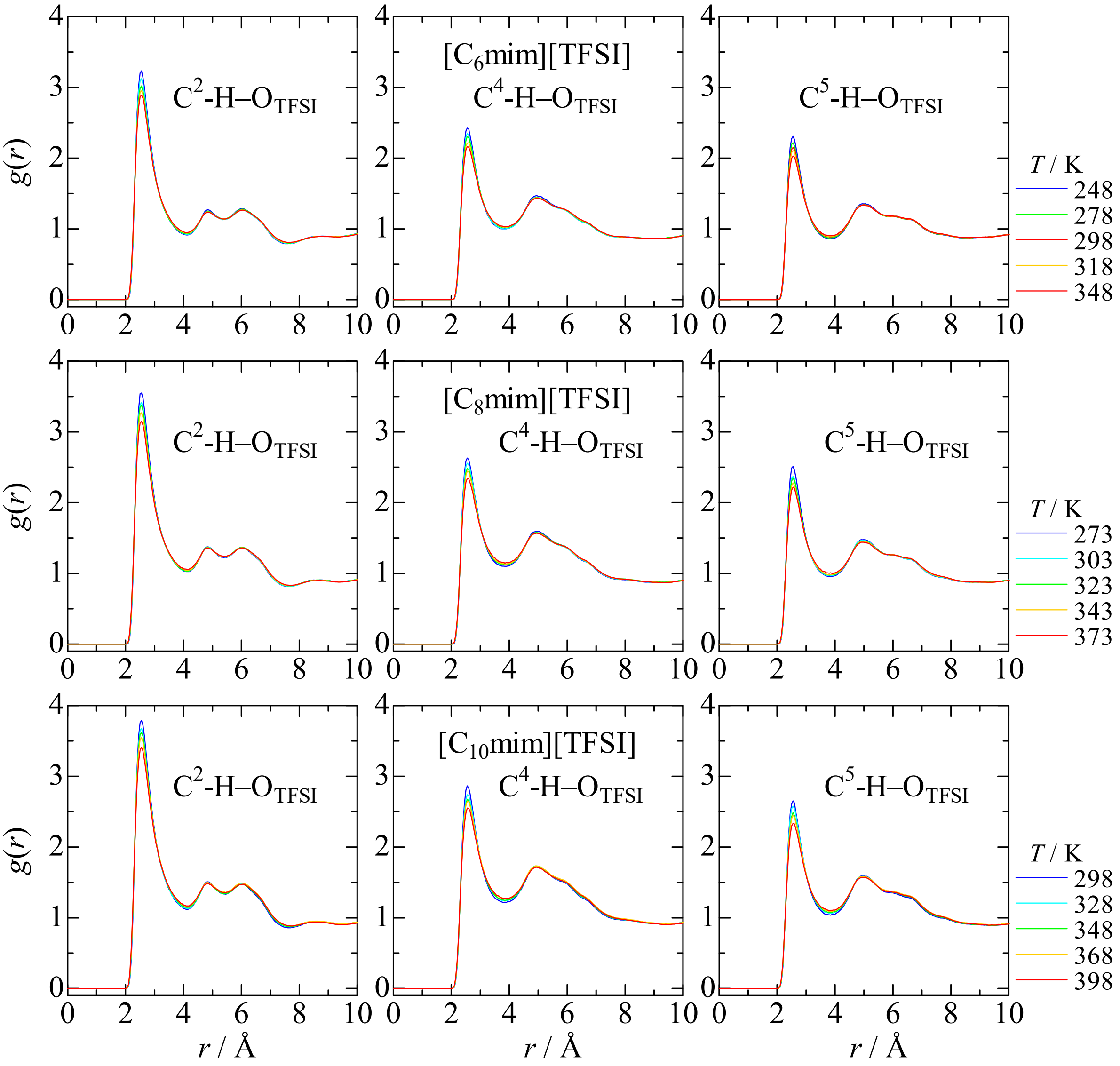

Fig. S22 Temperature dependence of MD pair correlation functions, $g(r)$s, for the C^{2,4,5}-H–O$_{\mathrm{TFSI}}$ interactions in neat [C$_n$mim][TFSI] systems (top: $n = 6$, middle: $n = 8$, and bottom $n = 10$, respectively). The $g(r)$s of the C^{2,4,5}-H–O$_{\mathrm{TFSI}}$ interactions were calculated for one of the four O atoms within [TFSI]$^-$.

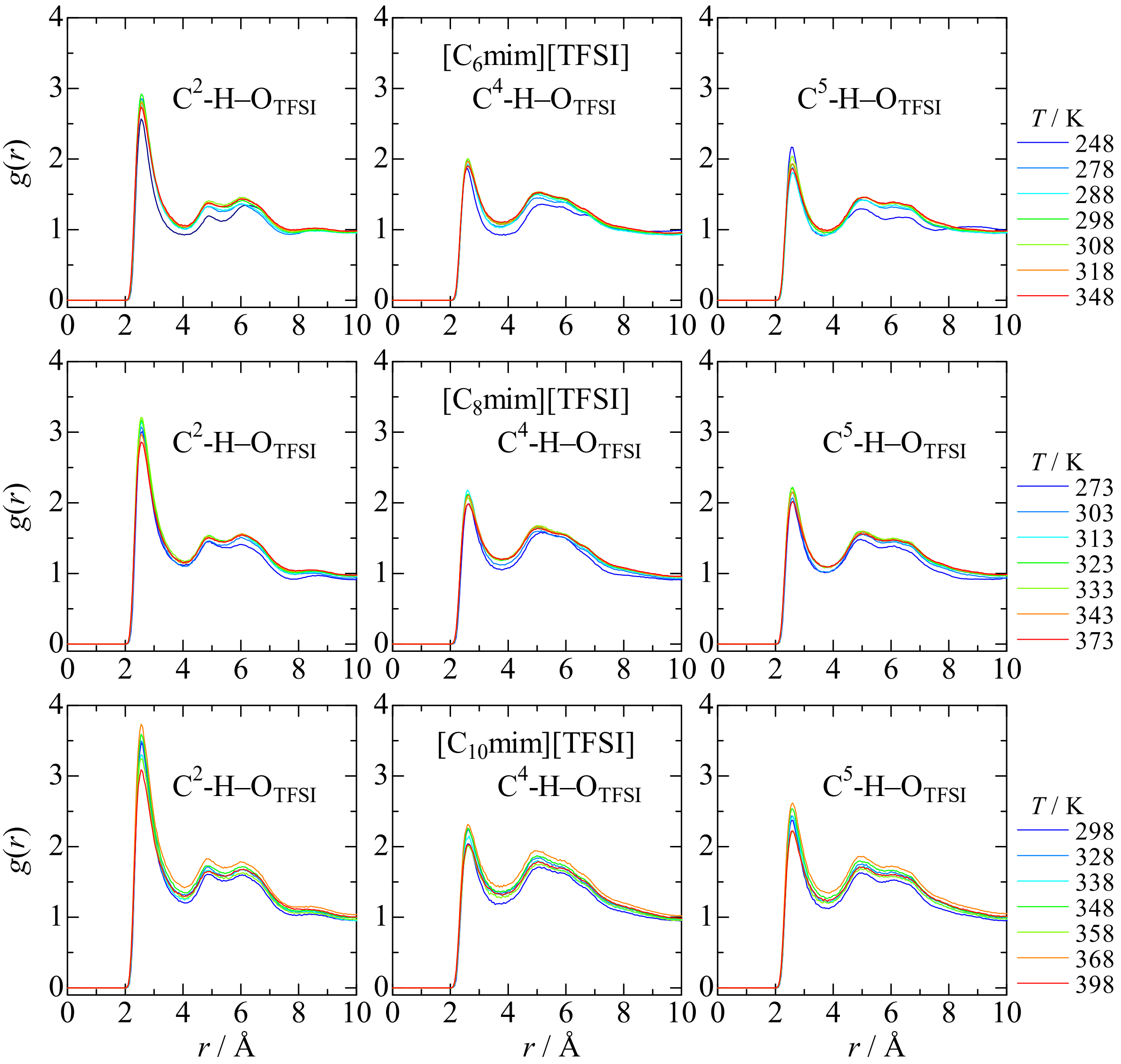

Fig. S23 Temperature dependence of MD pair correlation functions, $g(r)$s, for the C^{2,4,5}-H–O$_{\mathrm{TFSI}}$ interactions in [C$_n$mim][TFSI]–FA solutions (top: n = 6, middle: n = 8, and bottom n = 10, respectively) at each UCST composition (x_{FA} = 0.881, 0.900, and 0.926, respectively). The $g(r)$s of the C^{2,4,5}-H–O$_{\mathrm{TFSI}}$ interactions were calculated for one of the four O atoms within [TFSI]$^-$.

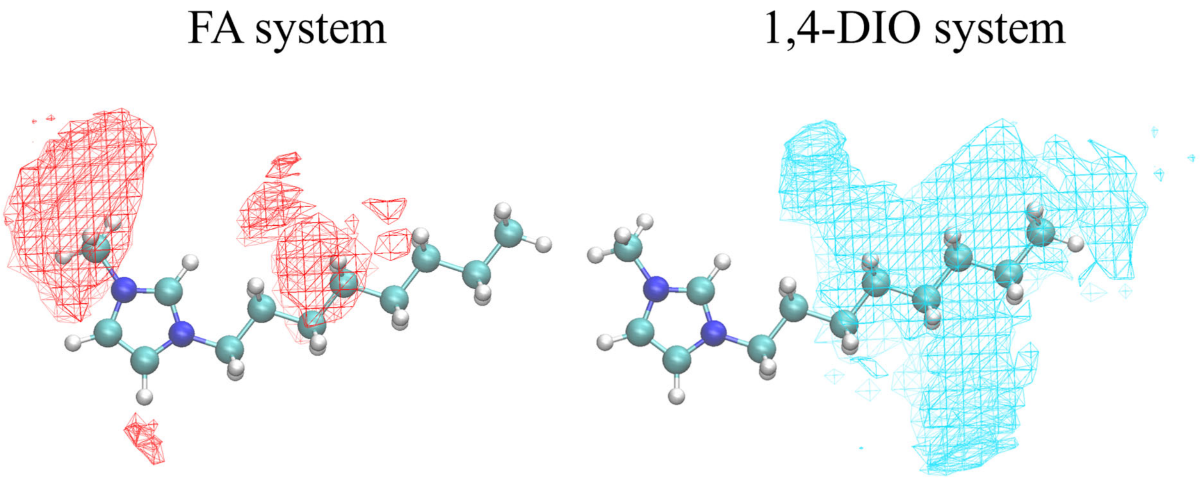

Fig.S24 MD spatial distribution functions (SDFs) for the center of mass of FA (red meshes) and 1,4-DIO (light-blue meshes) around $[C_8mim]^+$ in $[C_8mim][TFSI]$–FA (left) and −1,4-DIO (right) solutions at x_{FA}= 0.900 and 343.2 K and $x_{1,4\text{-DIO}}$ = 0.983 and 323.2 K, respectively.

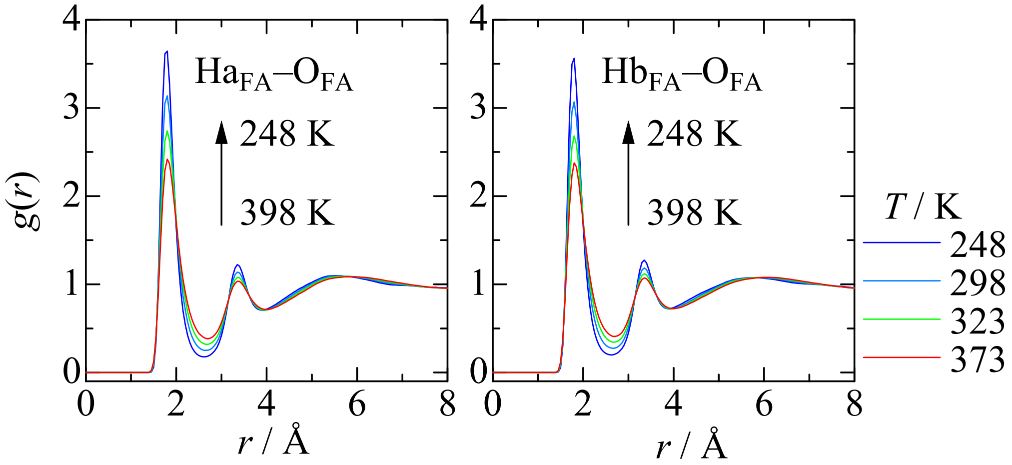

Fig. S25 Temperature dependence of MD pair correlation functions, $g(r)$s, for the Ha_{FA}–O_{FA} (left) and the Hb_{FA}–O_{FA} (right) interactions in neat FA.

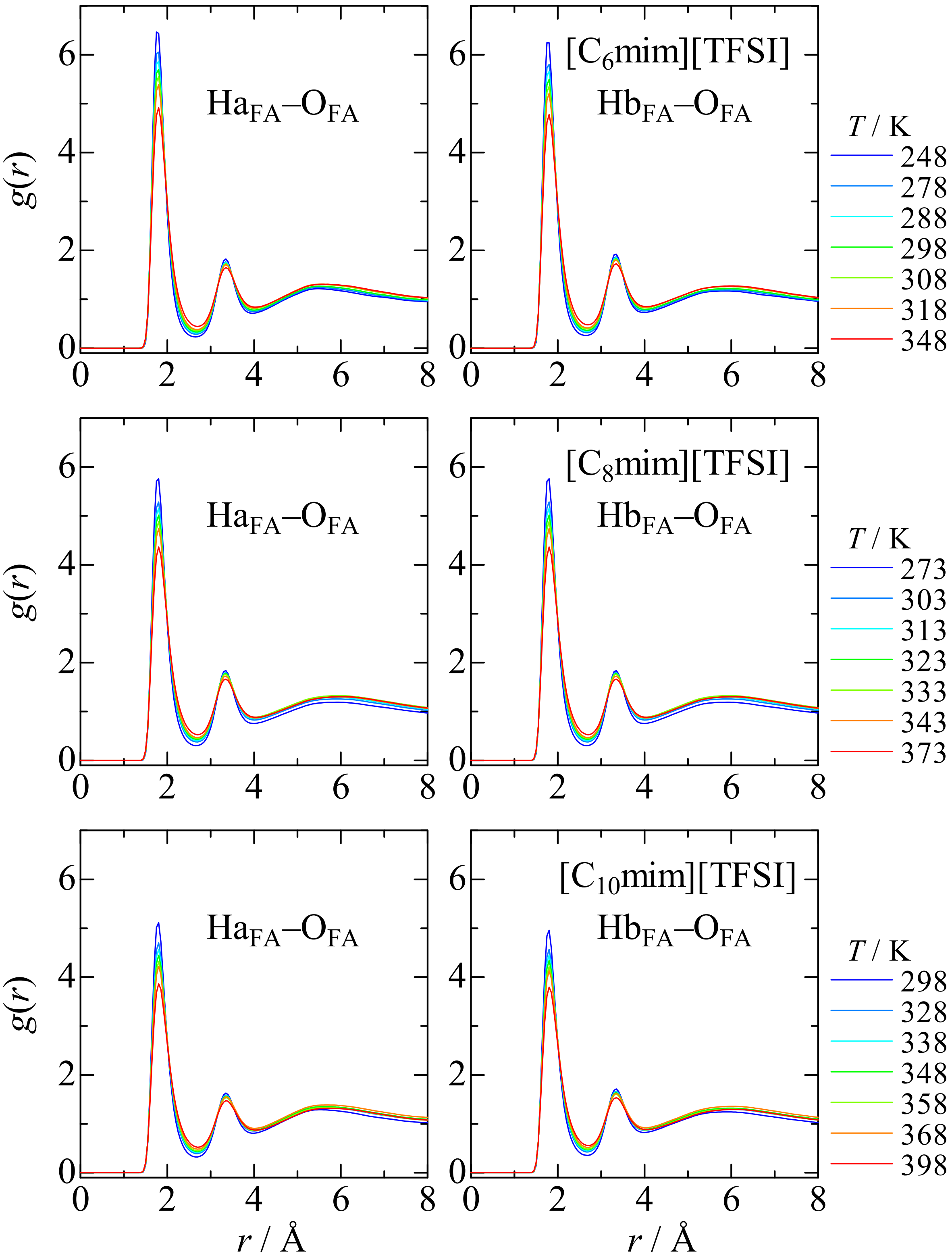

Fig. S26 Temperature dependence of MD pair correlation functions, $g(r)$s, for the Ha$_{FA}$–O$_{FA}$ (left) and the Hb$_{FA}$–O$_{FA}$ (right) interactions in [C$_n$mim][TFSI]–FA solutions (top: $n = 6$, middle: $n = 8$, and bottom: $n = 10$) at the UCST compositions ($n = 6$, 8, and 10, $x_{FA} = 0.881$, 0.900, and 0.926, respectively).

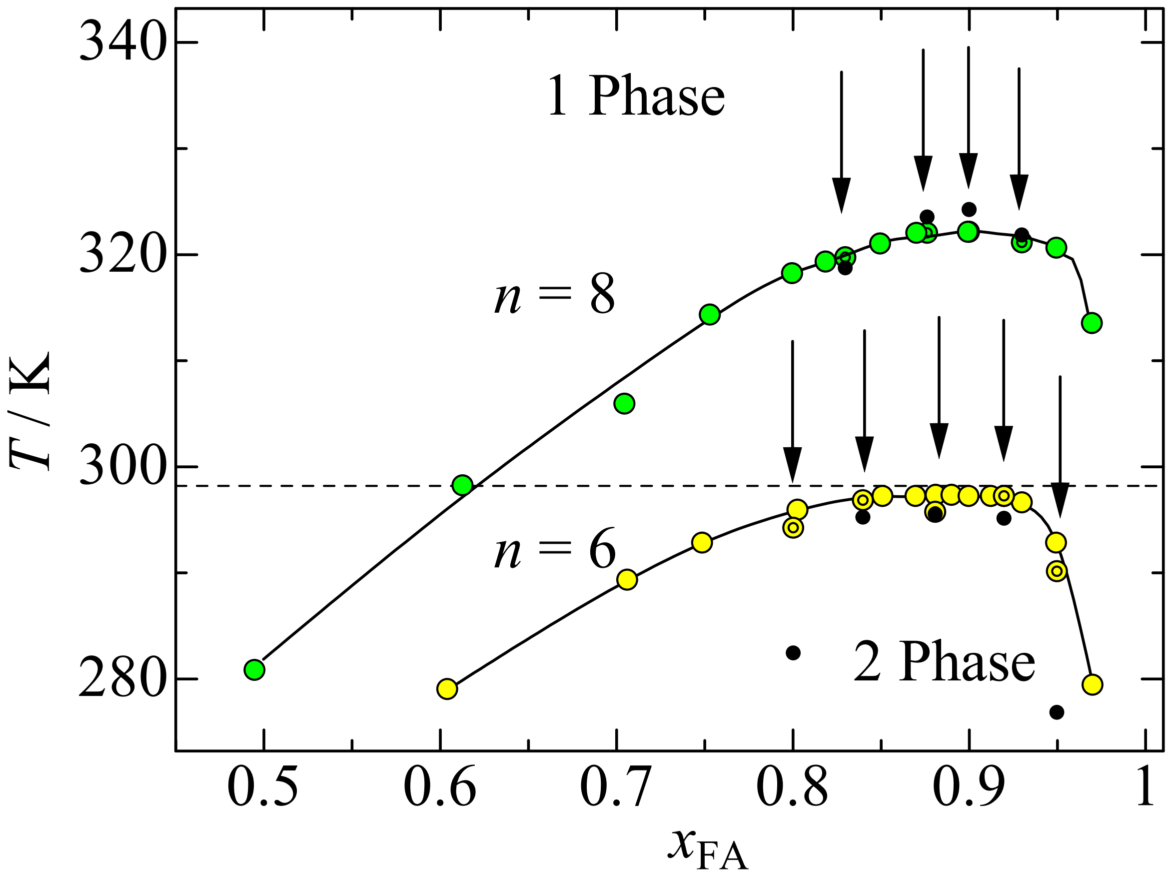

Fig. S27 Phase diagrams of [C$_n$mim][TFSI]–FA (n = 6, and 8) and [C$_n$mim][TFSI]–FA-d_2 systems. The single and double circles represent the experimental binodal temperatures for [C$_n$mim][TFSI]–FA and –FA-d_2 systems, respectively. The solid lines are guide for eyes. The horizontal broken line indicates 298.2 K. The SANS experiments for [C$_6$mim][TFSI]–FA-d_2 systems at $x_{\text{FA-}d2}$ = 0.800, 0.840, 0.881, 0.920, and 0.950 and [C$_8$mim][TFSI]–FA-d_2 systems at $x_{\text{FA-}d2}$ = 0.830, 0.876, 0.900, and 0.930 were made with lowering temperature along the arrows. Dots give spinodal temperatures T_s for [C$_n$mim][TFSI]–FA-d_2 systems estimated using eqns (S1) and (S2).

Table S7 Ornstein–Zernike correlation lengths ξ and scattering intensities I_0 determined by SANS experiments for [C$_6$mim][TFSI]–FA-d_2 solutions at $x_{\text{FA-}d2}$ = 0.800, 0.840, 0.881, 0.920, and 0.950 and various temperatures.[a]

[C$_6$mim][TFSI]–FA-d_2							
$x_{\text{FA-d}2}$	T / K	ξ / Å	I_0 / cm^{-1}	$x_{\text{FA-d}2}$	T / K	ξ / Å	I_0 / cm^{-1}
0.800	293.2	27.4(2)	1.386(8)	0.881	296.7	78.0(7)	14.9(1)
	293.7	26.1(2)	1.275(5)		297.2	65.6(6)	10.57(9)
	294.0	25.1(2)	1.190(5)		297.7	55.8(7)	7.54(7)
	294.2	24.7(1)	1.135(4)		298.2	48.2(4)	5.86(4)
	294.4	24.1(2)	1.077(6)		300.2	34.3(2)	3.013(1)
	294.7	23.1(2)	1.010(5)		303.2	25.8(2)	1.685(6)
	295.2	22.2(2)	0.930(6)		308.2	19.8(2)	0.948(5)
	295.7	20.8(1)	0.829(4)		313.2	16.9(2)	0.655(5)
	296.2	20.0(1)	0.772(3)		318.2	14.9(2)	0.503(4)
	297.2	18.9(1)	0.671(3)	0.920	296.2	65.3(5)	8.79(8)
	298.2	17.8(2)	0.600(4)		296.5	54.5(2)	6.39(3)
	300.2	16.2(2)	0.487(3)		296.8	49.5(3)	5.28(3)
	303.2	14.4(2)	0.375(2)		297.0	46.4(2)	4.64(2)
	308.2	12.7(2)	0.281(2)		297.2	44.1(3)	4.26(2)
	313.2	11.6(3)	0.222(3)		297.4	42.4(3)	3.92(2)
	318.2	11.0(3)	0.188(2)		297.7	38.8(2)	3.32(1)
0.840	296.5	66.8(4)	9.15(5)		298.2	35.9(2)	2.86(1)
	296.8	58.7(3)	7.18(4)		299.2	30.9(1)	2.155(6)
	297.0	54.4(3)	6.25(3)		300.2	27.6(1)	1.739(6)
	297.2	51.0(3)	5.43(3)		303.2	22.3(1)	1.132(4)
	297.4	47.4(2)	4.78(2)		308.2	17.9(1)	0.715(3)
	297.7	43.3(3)	4.00(2)		313.2	15.4(2)	0.525(3)
	297.9	41.6(3)	3.67(2)		318.2	13.5(1)	0.409(2)
	298.2	37.8(2)	3.12(1)	0.950	290.2	17.9(1)	0.601(3)
	298.7	34.6(2)	2.60(1)		291.2	17.4(2)	0.547(3)
	299.2	32.0(2)	2.242(9)		292.2	16.6(2)	0.508(3)
	300.2	27.6(1)	1.703(5)		293.2	16.3(2)	0.476(4)
	303.2	21.7(2)	1.052(5)		294.2	15.7(2)	0.440(3)
	308.2	16.9(2)	0.647(5)		295.2	15.2(2)	0.422(3)
	313.2	14.3(2)	0.451(4)		298.2	14.1(2)	0.357(2)
	318.2	12.3(2)	0.347(3)		303.2	13.1(2)	0.290(2)
0.881	295.7	244.0(42)	140.6(38)		308.2	12.3(2)	0.251(3)
	295.9	154.6(15)	58.0(7)		313.2	11.6(2)	0.215(2)
	296.2	114.2(9)	31.6(3)		318.2	11.3(3)	0.195(2)

[a] The values in the parentheses are the estimated standard deviation σ of the last figure.

Table S8 Ornstein–Zernike correlation lengths ξ and scattering intensities I_0 determined by SANS experiments for [C_8mim][TFSI]–FA-d_2 solutions at $x_{\text{FA-}d2}$ = 0.830, 0.876, 0.900, and 0.930 and various temperatures.[a]

[C_8mim][TFSI]–FA-d_2							
$x_{\text{FA-d}2}$	T / K	ξ / Å	I_0 / cm^{-1}	$x_{\text{FA-d}2}$	T / K	ξ / Å	I_0 / cm^{-1}
0.830	322.2	28.4(2)	1.400(8)	0.900	324.2	764.51(5)	1395.90(1)
	323.2	27.1(2)	1.301(7)		325.2	91.6(7)	20.5(2)
	325.2	21.5(2)	0.874(6)		326.2	60.3(5)	9.19(7)
	328.2	17.8(2)	0.593(4)		328.2	38.4(2)	3.95(1)
	330.2	15.5(2)	0.478(3)		330.2	30.2(2)	2.45(9)
	333.2	13.9(2)	0.369(3)		333.2	23.7(1)	1.51(5)
	338.2	11.7(2)	0.280(3)		338.2	17.9(1)	0.878(3)
	343.2	10.6(2)	0.241(2)		343.2	15.4(1)	0.654(3)
0.876	324.2	127.7(21)	28.0(6)	0.930	323.2	82.1(5)	15.52(9)
	325.2	78.3(6)	12.3(1)		324.2	67.1(4)	11.24(7)
	326.2	53.8(4)	5.98(4)		326.2	39.7(3)	4.17(3)
	328.2	36.1(2)	2.81(1)		328.2	30.5(2)	2.49(1)
	330.2	29.0(2)	1.793(8)		330.2	25.5(1)	1.768(5)
	333.2	22.5(1)	1.122(3)		333.2	21.4(2)	1.247(7)
	338.2	17.8(2)	0.689(4)		338.2	17.7(1)	0.875(3)
	343.2	14.8(2)	0.514(3)		343.2	15.1(1)	0.652(3)

[a] The values in the parentheses are the estimated standard deviation σ of the last figure.

S3.3 Mechanism of phase separation from SANS measurements

To discuss the mechanism of phase separation of the [C$_n$mim][TFSI]–FA-d_2 solutions at various $x_{\text{FA-}d2}$ examined, firstly, the spinodal temperatures T_s were tentatively estimated from the I_0 and ξ values obtained from the SANS profiles through the following equations,

$$I_0^{-1} = C_1 \left|\frac{T-T_\text{s}}{T_\text{s}}\right|^{\gamma}, \tag{S1}$$

$$\xi^{-1} = C_2 \left|\frac{T-T_\text{s}}{T_\text{s}}\right|^{\nu}, \tag{S2}$$

where C_1 and C_2 are constant values, $(T - T_\text{s})/T_\text{s}$ is the normalized temperature, and γ and ν are the critical exponents. Tentatively, γ and ν values were fixed using typical values for 3D-Ising ($\gamma = 1.24$ and $\nu = 0.63$) or mean field ($\gamma = 1.00$ and $\nu = 0.50$). Then, T_s values were estimated from fits for the plots of I_0^{-1} and ξ^{-1} against temperature using eqns (S1) and (S2), respectively, as shown in Fig. S28–S36. For cautious estimations, two temperature T ranges were employed because T_s is the key value to assign the mechanism of phase separation; the whole T range examined and the partial one near the phase separation temperature. The sum of squared errors of the fits for the [C$_6$mim][TFSI]–FA-d_2 and [C$_8$mim][TFSI]–FA-d_2 systems in the whole and partial T ranges are summarized in Tables S9 and S10, respectively.

For the [C$_6$mim][TFSI]–FA-d_2 system, as shown in Fig. S28–S32 and Table S9, the sums of squared errors at both sides of the UCST $x_{\text{FA-}d2}$ ($x_{\text{FA-}d2} = 0.881$) in the whole and partial T ranges for the mean field model are significantly smaller than those for the 3D-Ising model. On the other hand, the values at the UCST $_{\text{FA-}d2}$ in both T ranges for the 3D-Ising are smaller compared to those for the mean field, except for the ξ^{-1} values in the whole T range. These results suggest that phase separation of the [C$_6$mim][TFSI]–FA-d_2 solution only at the UCST $x_{\text{FA-}d2}$ occurs in the 3D-Ising mechanism, while that at the other mole fractions in the mean field one.

For the [C$_8$mim][TFSI]–FA-d_2 system, the fits and their sums of squared errors are compared in Fig. S33–S36 and Table S10. In the whole T range, the sums of squared errors for both I_0^{-1}

and ξ^{-1} values at $x_{\text{FA-}d2} = 0.830$, which is far from the UCST $x_{\text{FA-}d2}$, for the mean field model are smaller than those for the 3D-Ising model. The fits on the ξ^{-1} values at $x_{\text{FA-}d2} = 0.900$, 0.876, and 0.930, which are the UCST $x_{\text{FA-}d2}$ and its both sides, respectively, in the whole T range reveal the 3D-Ising mechanism. In contrast, the sums of squared errors for the I_0^{-1} values at the mole fractions in the whole T range suggest the mean field mechanism. The errors for both I_0^{-1} and ξ^{-1} values at all $x_{\text{FA-}d2}$ in the partial T range for the 3D-Ising model are much smaller than those for the mean field. These ambiguities for the [C$_8$mim][TFSI]–FA-d_2 solutions around the UCST $x_{\text{FA-}d2}$ imply that the enhancement of the microheterogeneity of the solutions upon cooling progresses in the mean field mechanism far from the phase separation temperature, but in the 3D-Ising mechanism near the temperature.

Using the T_s ($T_{\text{s 3D-Ising}}$ and $T_{\text{s mean field}}$) values estimated above (Tables S11–S14), the phase separation mechanisms for the [C$_6$mim][TFSI]– and [C$_8$mim][TFSI]–FA-d_2 systems were decided by following. The critical exponents of γ and ν of phase separation for the solution at each $x_{\text{FA-}d2}$ were determined from fits for the temperature dependence of I_0 and ξ using equations,

$$I_0 = I_{\text{bare}} \left|\frac{T - T_\text{s}}{T_\text{s}}\right|^{-\gamma}, \tag{S3}$$

$$\xi = \xi_{\text{bare}} \left|\frac{T - T_\text{s}}{T_\text{s}}\right|^{-\nu}, \tag{S4}$$

where I_{bare} and ξ_{bare} are the bare I_0 and ξ, respectively. The analyses of Cases 1 and 2 for both solutions were made using the $T_{\text{s 3D-Ising}}$ and $T_{\text{s mean field}}$ values for the whole T range, respectively. In contrast, those of Cases 3 and 4 were conducted using the values for the partial T range near the phase separation temperature, respectively.

The γ and ν values estimated for the [C$_6$mim][TFSI]–FA-d_2 solutions in the whole and partial T ranges are summarized in Tables S11 and S12, respectively. In the tables, the differences between the critical exponent of γ or ν and each typical value (1.24 and 0.63 for the 3D-Ising and 1.00 and 0.50 for the mean field) are also given. The suitability of the phase separation mechanism with the smaller difference is described in the last column of the tables. According to the sums of squared errors for the estimation of T_s (Table S9) and the suitability (Tables S11 and S12), we can decide that phase separation of the [C$_6$mim][TFSI]–FA-d_2 solutions at $x_{\text{FA-}d2}$ = 0.800, 0.920, and 0.950 takes place via the mean field mechanism. However, the suitability for the solution at the UCST $x_{\text{FA-}d2}$ of 0.881 and its neighbor of 0.840 for the whole T range (Table S11) suggests the mean field mechanism, whereas that for the partial T range (Table S12) reveals the 3D-Ising mechanism, as depicted in *the Italic characters* in the tables. In such case, we give the priority to the candidate for the partial T range near each phase separation temperature. Therefore, phase separation of the solutions at the UCST $x_{\text{FA-}d2}$ and its vicinity occurs via the 3D-Ising mechanism.

The critical exponents of γ and ν and the differences for the [C$_8$mim][TFSI]–FA-d_2 solutions for the whole and partial T ranges are summarized in Tables S13 and S14, respectively. The suitability of the solutions at the UCST $x_{\text{FA-}d2}$ of 0.900 and its both sides of 0.876 and 0.930 gives the 3D-Ising mechanism. This is consistent with the candidate from the estimation for T_s values in the partial T range (Table S10), although the fits for the I_0^{-1} values in the whole range suggest the mean field. Thus, we conclude the 3D-Ising for the phase separation mechanism of the three solutions around the UCST $x_{\text{FA-}d2}$. On the other hand, the suitability of the solution at $x_{\text{FA-}d2}$ = 0.830 in the whole T range reveals the mean field, while that in the partial T range shows the 3D-Ising. According to the priority for the partial T range as the above, we decide the 3D-Ising mechanism for the solution at $x_{\text{FA-}d2}$ = 0.830. Therefore, phase separation of the [C$_8$mim][TFSI]–FA-d_2 solutions at all the mole fractions examined occurs via the 3D-Ising mechanism.

For the present [C$_n$mim][TFSI]–FA-d_2 solutions, the temperature range dependence of the suitability for the phase separation mechanisms is found, unlike the previous

[C$_8$mim][TFSI]–1,4-DIO-d_8 solutions. It is likely that the crossover of the mechanism for the enhancement of heterogeneity from the mean field to the 3D-Ising occurs for the FA solutions against temperature due to the strong self-hydrogen bonding among FA.

The final decision for the mechanism of the [C$_6$mim][TFSI]–FA-d_2 and [C$_8$mim][TFSI]–FA-d_2 solutions, together with the final T_s values and the critical exponents of γ and ν, are summarized in Table 2 of the main text. To reconfirm the mechanism concluded for each solution, the I_0 and ξ values were plotted as a function of $(T - T_s)/T_s$ using the final T_s in Fig. S37. This figure proves the validities of all the classification for the phase separation mechanisms.

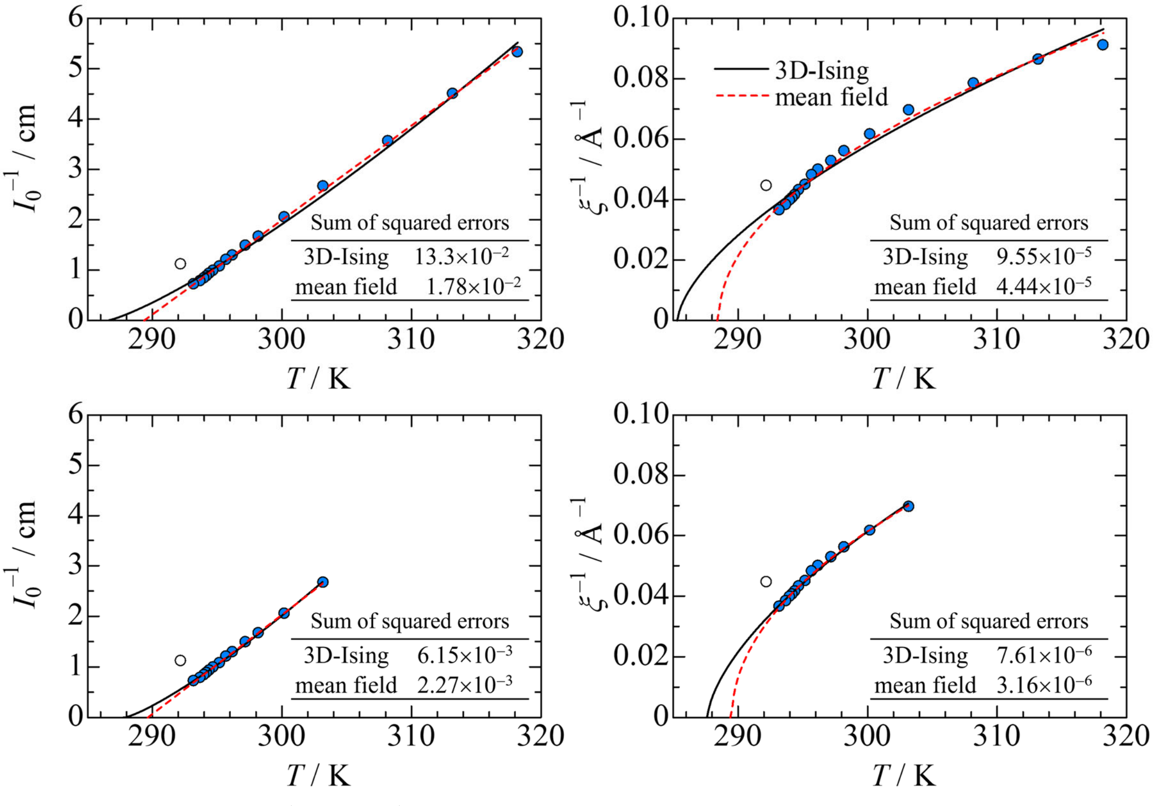

Fig. S28 Fitting for I_0^{-1} and ξ^{-1} values of [C$_6$mim][TFSI]–FA-d_2 solution at $x_{\text{FA-}d2}$ = 0.800 against T in the whole range examined (upper) and the partial range near phase separation temperature (bottom). Solid and dashed lines show the results of fits with the assumption of 3D-Ising and mean field models, respectively, using eqns (S1) and (S2). White circles give the values estimated from SANS profiles for the sample solution after phase separation and were not used for the fits to determine T_s. The sums of squared errors of the fits by eqns (S1) and (S2) are inserted in the figures.

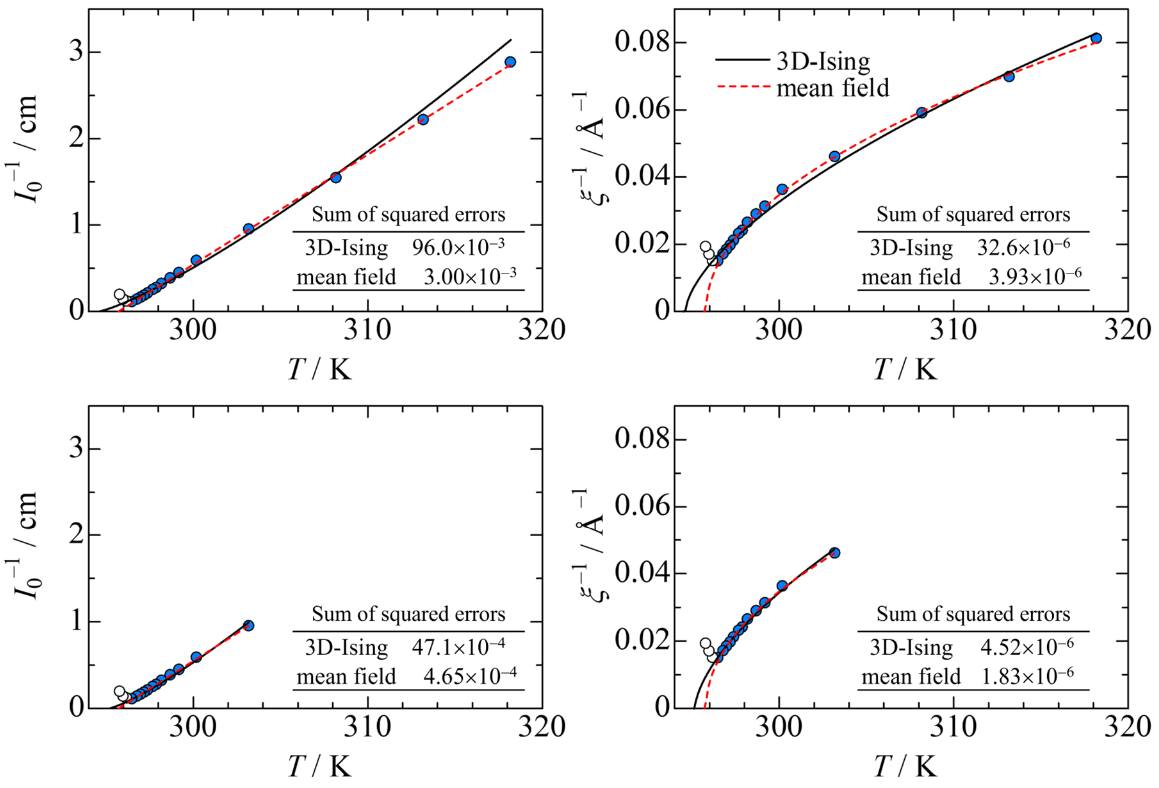

Fig. S29 Fitting for I_0^{-1} and ξ^{-1} values of [C$_6$mim][TFSI]–FA-d_2 solution at $x_{\text{FA-}d2}$ = 0.840 against T in the whole range examined (upper) and the partial range near phase separation temperature (bottom). The types of lines and circles are the same as those in Fig. S28.

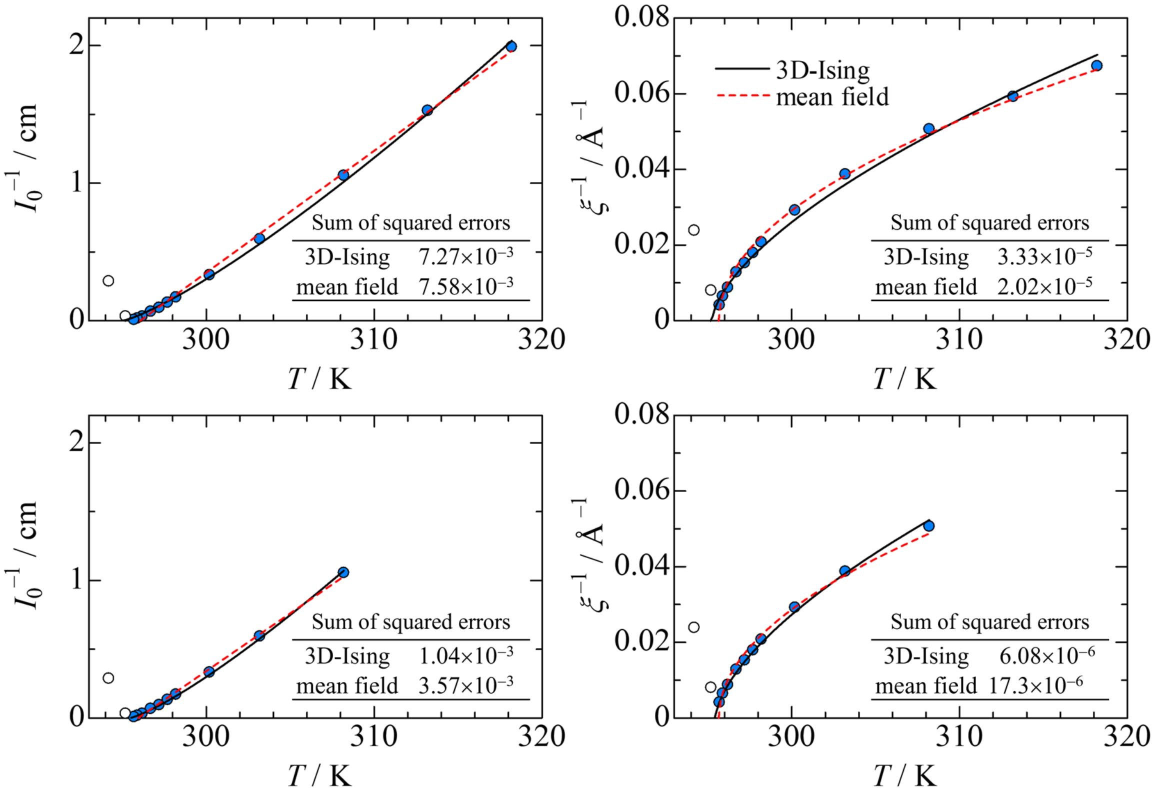

Fig. S30 Fitting for I_0^{-1} and ξ^{-1} values of [C$_6$mim][TFSI]–FA-d_2 solution at $x_{\text{FA-}d2}$ = 0.881 against T in the whole range examined (upper) and the partial range near phase separation temperature (bottom). The types of lines and circles are the same as those in Fig. S28.

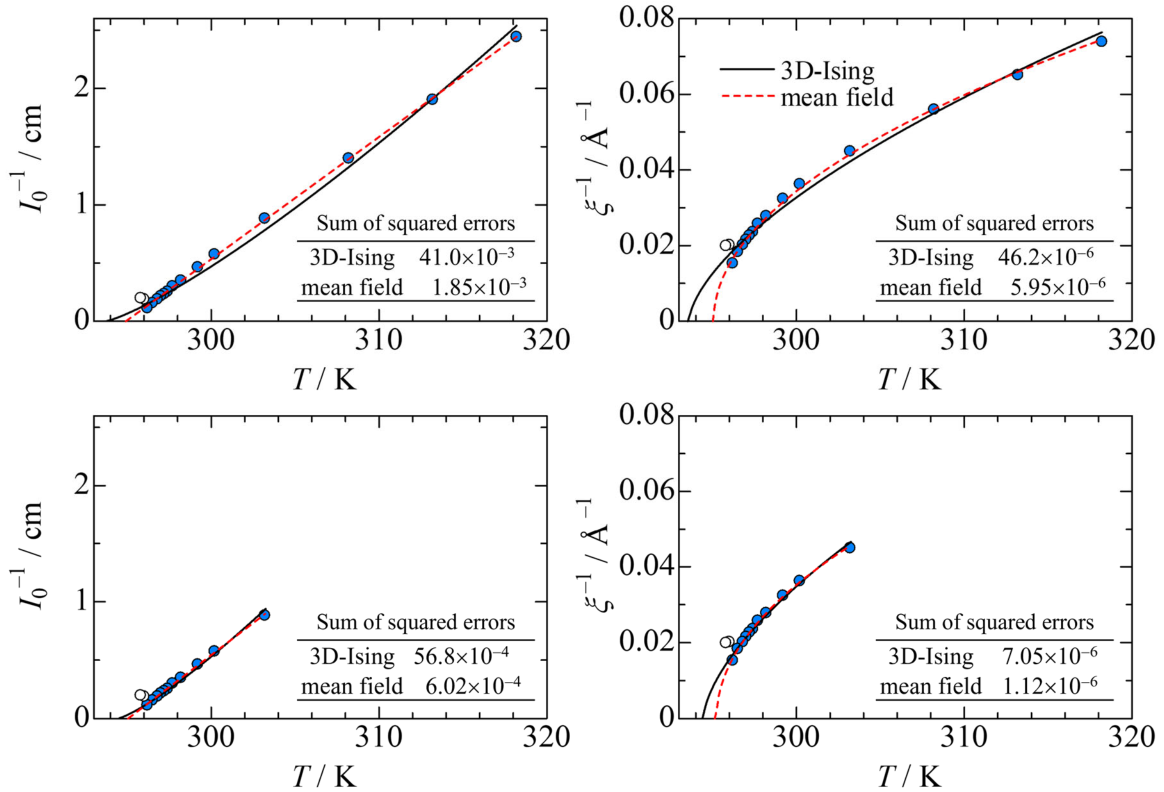

Fig. S31 Fitting for I_0^{-1} and ξ^{-1} values of [C$_6$mim][TFSI]–FA-d_2 solution at $x_{\text{FA-}d2}$ = 0.920 against T in the whole range examined (upper) and the partial range near phase separation temperature (bottom). The types of lines and circles are the same as those in Fig. S28.

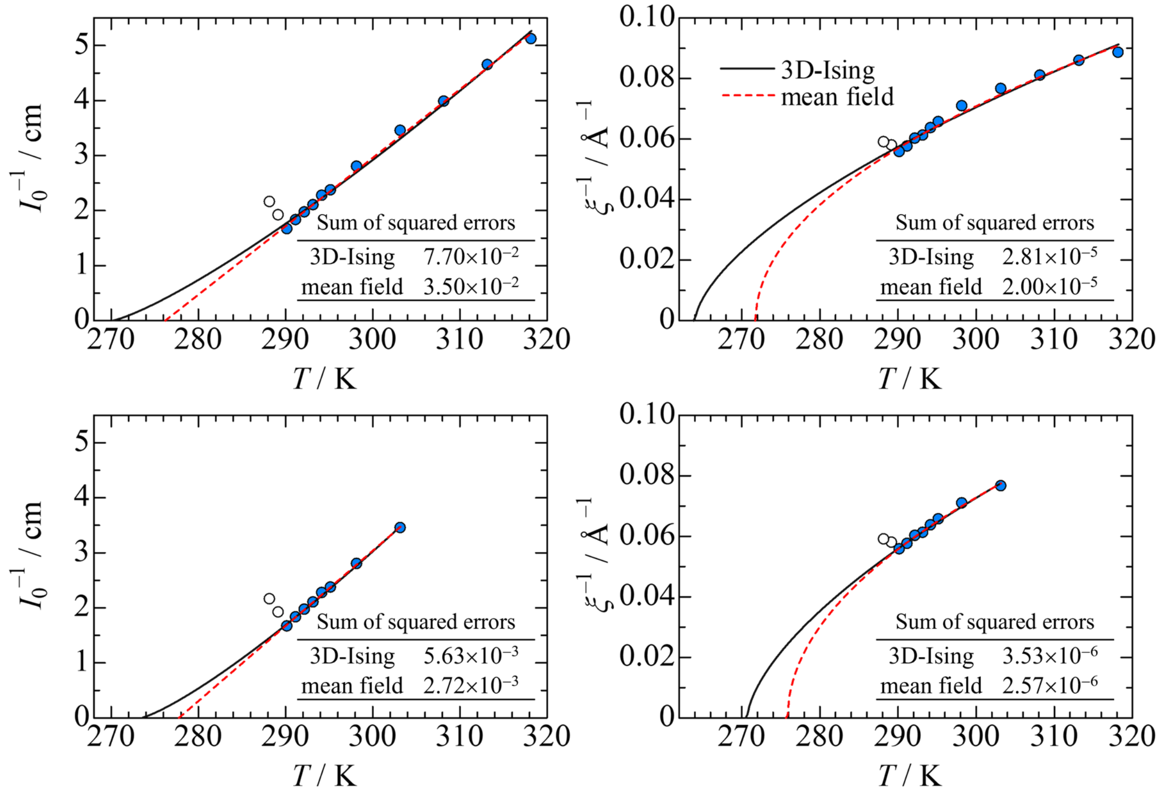

Fig. S32 Fitting for I_0^{-1} and ξ^{-1} values of [C$_6$mim][TFSI]–FA-d_2 solution at $x_{\text{FA-}d2}$ = 0.950 against T in the whole range examined (upper) and the partial range near phase separation temperature (bottom). The types of lines and circles are the same as those in Fig. S28.

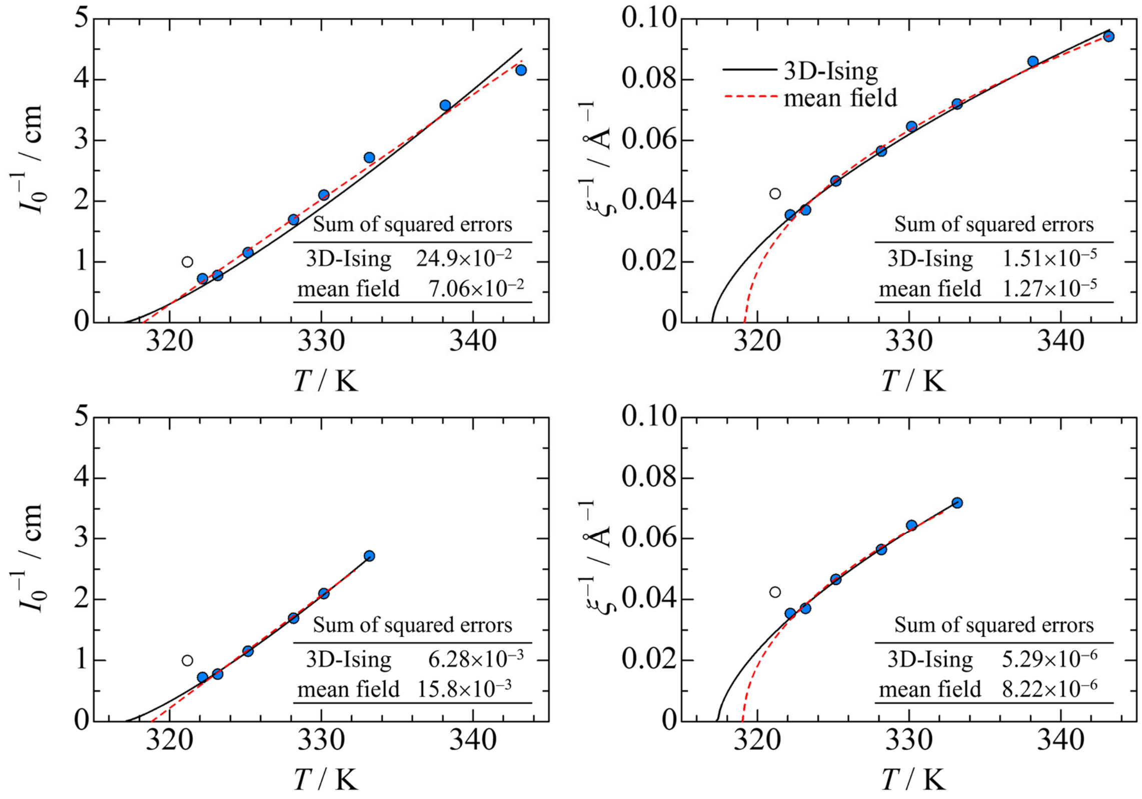

Fig. S33 Fitting for I_0^{-1} and ξ^{-1} values of [C$_8$mim][TFSI]–FA-d_2 solution at $x_{\text{FA-}d2}$ = 0.830 against T in the whole range examined (upper) and the partial range near phase separation temperature (bottom). The types of lines and circles are the same as those in Fig. S28.

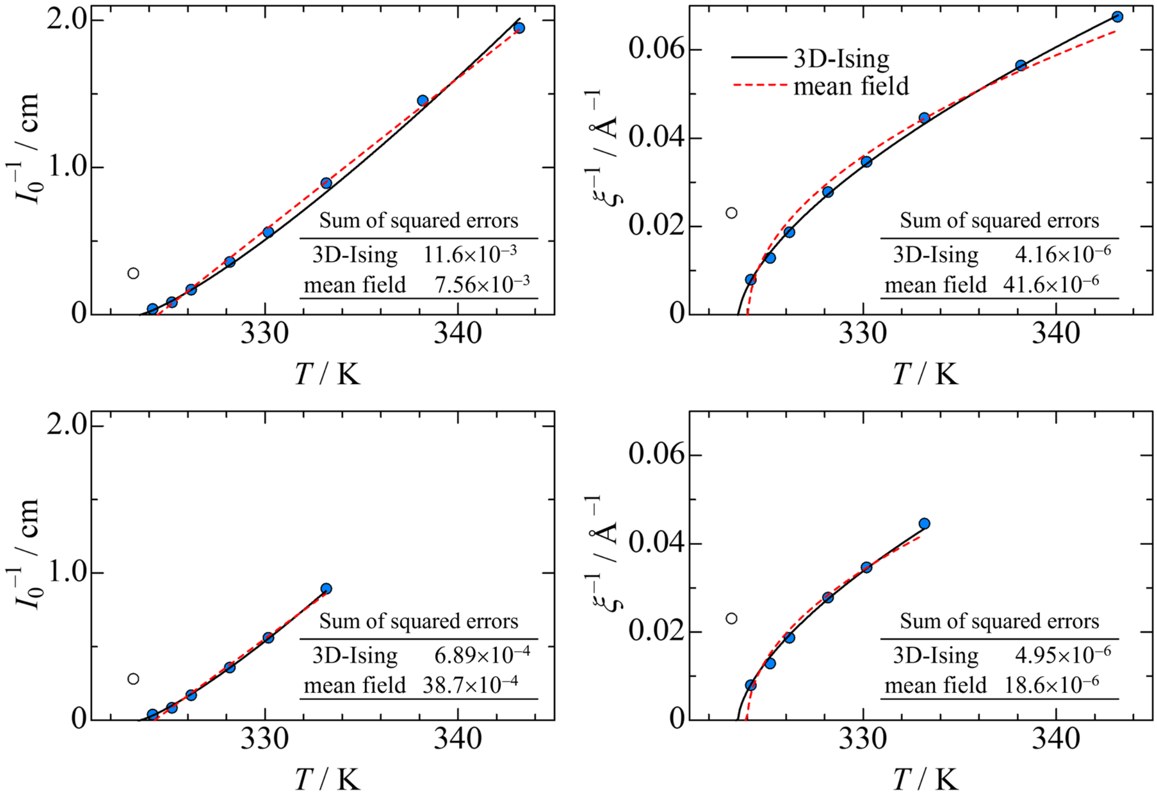

Fig. S34 Fitting for I_0^{-1} and ξ^{-1} values of [C$_8$mim][TFSI]–FA-d_2 solution at $x_{\text{FA-}d2}$ = 0.876 against T in the whole range examined (upper) and the partial range near phase separation temperature (bottom). The types of lines and circles are the same as those in Fig. S28.

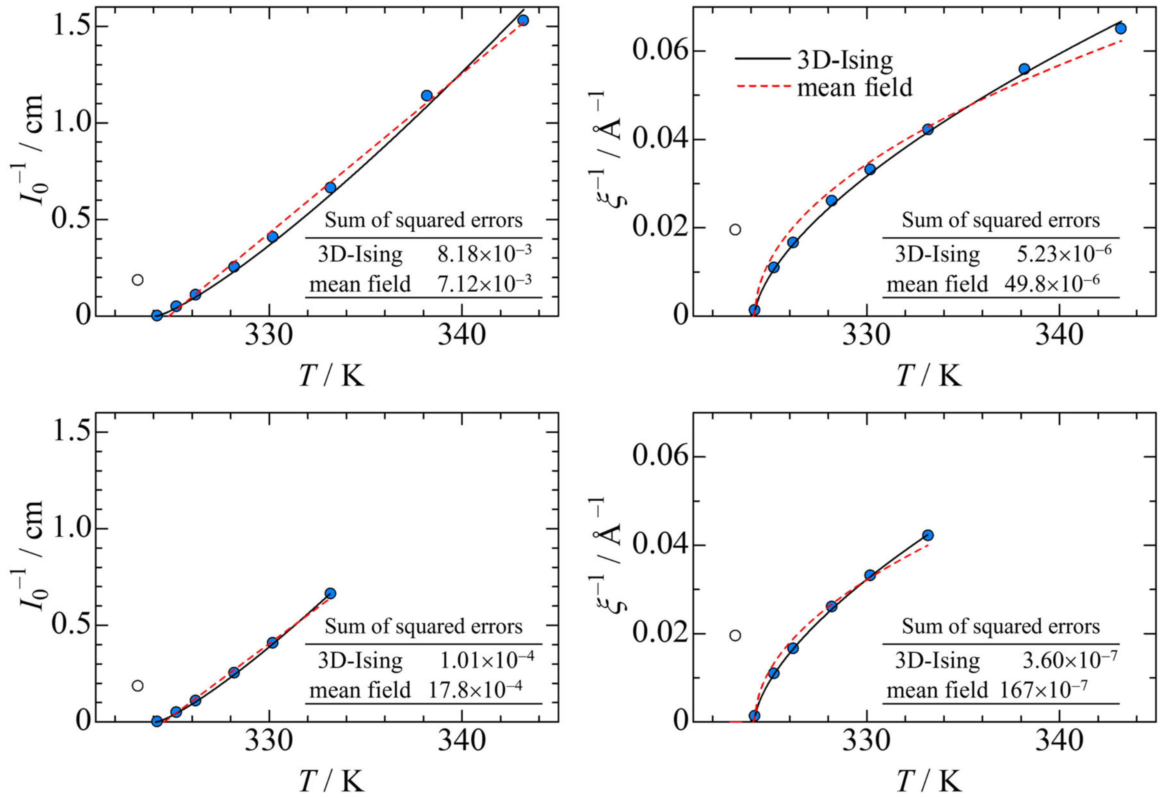

Fig. S35 Fitting for I_0^{-1} and ξ^{-1} values of [C$_8$mim][TFSI]–FA-d_2 solution at $x_{\text{FA-}d2}$ = 0.900 against T in the whole range examined (upper) and the partial range near phase separation temperature (bottom). The types of lines and circles are the same as those in Fig. S28.

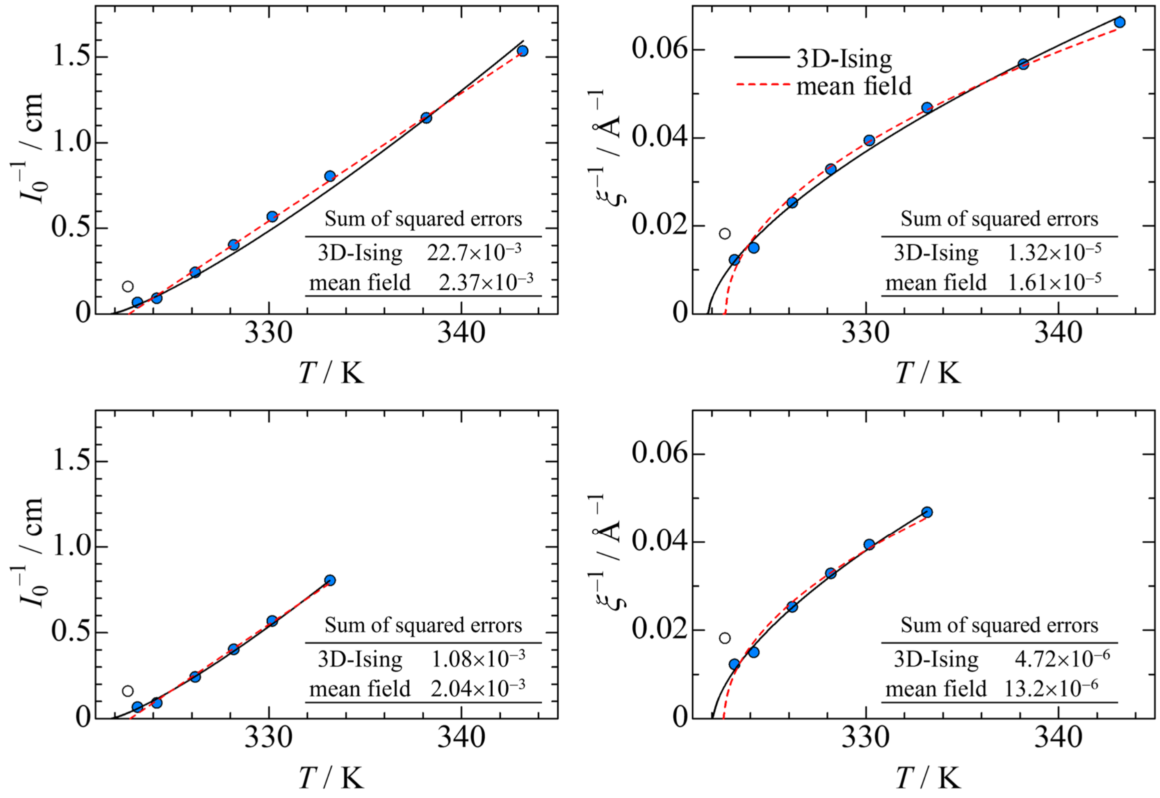

Fig. S36 Fitting for I_0^{-1} and ξ^{-1} values of [C$_8$mim][TFSI]–FA-d_2 solution at $x_{\text{FA-}d2}$ = 0.930 against T in the whole range examined (upper) and the partial range near phase separation temperature (bottom). The types of lines and circles are the same as those in Fig. S28.

Table S9 Sum of squared errors of the T_s fits of [C$_6$mim][TFSI]–FA-d_2 solutions at various $x_{\text{FA-}d2}$, respectively, with T_s estimated from the whole and partial T ranges of Fig. S28–S32.

	Sum of squared errors for whole T range			
	I_0^{-1}		ξ^{-1}	
$x_{\text{FA-}d2}$	3D-Ising	mean field	3D-Ising	mean field
0.800	13.3×10^{-2}	1.78×10^{-2}	9.55×10^{-5}	4.44×10^{-5}
0.840	96.0×10^{-3}	3.00×10^{-3}	32.6×10^{-6}	3.93×10^{-6}
0.881*	7.27×10^{-3}	7.58×10^{-3}	3.33×10^{-5}	2.02×10^{-5}
0.920	41.0×10^{-3}	1.85×10^{-3}	46.2×10^{-6}	5.95×10^{-6}
0.950	7.70×10^{-2}	3.50×10^{-2}	2.81×10^{-5}	2.00×10^{-5}
	Sum of squared errors for partial T range			
	I_0^{-1}		ξ^{-1}	
$x_{\text{FA-}d2}$	3D-Ising	mean field	3D-Ising	mean field
0.800	6.15×10^{-3}	2.27×10^{-3}	7.61×10^{-6}	3.16×10^{-6}
0.840	47.1×10^{-4}	4.65×10^{-4}	4.52×10^{-6}	1.83×10^{-6}
0.881*	1.04×10^{-3}	3.57×10^{-3}	6.08×10^{-6}	17.3×10^{-6}
0.920	56.8×10^{-4}	6.02×10^{-4}	7.05×10^{-6}	1.12×10^{-6}
0.950	5.63×10^{-3}	2.72×10^{-3}	3.53×10^{-6}	2.57×10^{-6}

*$x_{\text{FA-}d2}$ of the UCST composition.

Table S10 Sum of squared errors of the T_s fits of [C$_8$mim][TFSI]–FA-d_2 solutions at various $x_{\text{FA-}d2}$, respectively, with T_s estimated from the whole and partial T ranges of Fig. S33–S36.

	Sum of squared errors for whole T range			
	I_0^{-1}		ξ^{-1}	
$x_{\text{FA-}d2}$	3D-Ising	mean field	3D-Ising	mean field
0.830	24.9×10^{-2}	7.06×10^{-2}	1.51×10^{-5}	1.27×10^{-5}
0.876	11.6×10^{-3}	7.56×10^{-3}	4.16×10^{-6}	41.6×10^{-6}
0.900*	8.18×10^{-3}	7.12×10^{-3}	5.23×10^{-6}	49.8×10^{-6}
0.930	22.7×10^{-3}	2.37×10^{-3}	1.32×10^{-5}	1.61×10^{-5}
	Sum of squared errors for partial T range			
	I_0^{-1}		ξ^{-1}	
$x_{\text{FA-}d2}$	3D-Ising	mean field	3D-Ising	mean field
0.830	6.28×10^{-3}	15.8×10^{-3}	5.29×10^{-6}	8.22×10^{-6}
0.876	6.89×10^{-4}	38.7×10^{-4}	4.95×10^{-6}	18.6×10^{-6}
0.900*	1.01×10^{-4}	17.8×10^{-4}	3.60×10^{-7}	167×10^{-7}
0.930	1.08×10^{-3}	2.04×10^{-3}	4.72×10^{-6}	13.2×10^{-6}

*$x_{\text{FA-}d2}$ of the UCST composition.

Table S11 Critical exponents of γ and ν determined from fits on I_0 and ξ values of [C$_6$mim][TFSI]–FA-d_2 solutions at various $x_{\text{FA-}d2}$, respectively, with T_s estimated from the whole T range of Fig. S28−S32. Differences give the values between the estimated critical exponents and the typical ones of γ (1.24 and 1.00) and ν (0.63 and 0.50). Suitability refers to which model better explains the I_0 and ξ values when comparing the results of Cases 1 and 2. The description of the model's name indicates the better explanation.

Case 1: T_s values estimated by assuming 3D-Ising model were used.

$x_{\text{FA-}d2}$	T range / K	$T_{\text{s 3D-Ising}}$ / K	γ	Difference from 1.24	ν	Difference from 0.63	Suitability
0.800	293.2–318.2	285.9	1.45	0.21	0.65	0.02	
0.840	296.2–318.2	294.6	1.45	0.21	0.69	0.06	
0.881*	295.7–318.2	295.1	1.56	0.32	0.84	0.21	
0.920	296.2–318.2	293.7	1.47	0.23	0.69	0.06	
0.950	290.2–318.2	267.1	1.44	0.20	0.60	-0.03	

Case 2: T_s values estimated by assuming mean field model were used.

$x_{\text{FA-}d2}$	T range / K	$T_{\text{s mean field}}$ / K	γ	Difference from 1.00	ν	Difference from 0.50	Suitability
0.800	293.2–318.2	288.9	1.08	0.08	0.50	0.00	mean field
0.840	296.2–318.2	295.8	0.93	-0.07	0.49	-0.01	*mean field*
0.881*	295.7–318.2	295.9	0.90	-0.10	0.47	-0.03	*mean field*
0.920	296.2–318.2	295.0	1.05	0.05	0.53	0.03	mean field
0.950	290.2–318.2	274.0	1.13	0.13	0.47	-0.03	mean field

*$x_{\text{FA-}d2}$ of the UCST composition.

Table S12 Critical exponents of γ and ν determined from fits on I_0 and ξ values of [C$_6$mim][TFSI]–FA-d_2 solutions at various $x_{\text{FA-}d2}$, respectively, with T_s estimated from the partial T range of Fig. S28−S32. Differences give the values between the estimated critical exponents and the typical ones of γ (1.24 and 1.00) and ν (0.63 and 0.50). Suitability refers to which model better explains the I_0 and ξ values when comparing the results of Cases 3 and 4. The description of the model's name indicates the better explanation.

Case 3: T_s values estimated by assuming 3D-Ising model were used.

$x_{\text{FA-}d2}$	T range / K	$T_{\text{s 3D-Ising}}$ / K	γ	Difference from 1.24	ν	Difference from 0.63	Suitability
0.800	293.2–303.2	287.8	1.29	0.05	0.64	0.01	
0.840	296.2–303.2	295.2	1.25	0.01	0.65	0.02	*3D-Ising*
0.881*	295.7–308.2	295.5	1.22	-0.02	0.61	-0.02	*3D-Ising*
0.920	296.2–303.2	294.5	1.32	0.08	0.67	0.04	
0.950	290.2–303.2	272.1	1.35	0.11	0.61	-0.02	

Case 4: T_s values estimated by assuming mean field model were used.

$x_{\text{FA-}d2}$	T range / K	$T_{\text{s mean field}}$ / K	γ	Difference from 1.00	ν	Difference from 0.50	Suitability
0.800	293.2–303.2	289.6	1.00	0.00	0.50	0.00	mean field
0.840	296.2–303.2	296.3	0.91	-0.09	0.49	-0.01	
0.881*	295.7–308.2	295.8	0.74	-0.26	0.40	-0.10	
0.920	296.2–303.2	295.1	1.04	0.04	0.54	0.04	mean field
0.950	290.2–303.2	276.8	1.07	0.07	0.48	-0.02	mean field

*$x_{\text{FA-}d2}$ of the UCST composition.

Table S13 Critical exponents of γ and ν determined from fits on I_0 and ξ values of [C$_8$mim][TFSI]–FA-d_2 solutions at various $x_{\text{FA-}d2}$, respectively, with T_s estimated from the whole T range of Fig. S33–S36. Differences give the values between the estimated critical exponents and the typical ones of γ (1.24 and 1.00) and ν (0.63 and 0.50). Suitability refers to which model better explains the I_0 and ξ values when comparing the results of Cases 1 and 2. The description of the model's name indicates the better explanation.

Case 1: T_s values estimated by assuming 3D-Ising model were used.

$x_{\text{FA-}d2}$	T range / K	$T_{\text{s 3D-Ising}}$ / K	γ	Difference from 1.24	ν	Difference from 0.63	Suitability
0.830	322.2–343.2	317.0	1.17	-0.07	0.64	0.01	
0.876	324.2–343.2	323.5	1.19	-0.05	0.66	0.03	3D-Ising
0.900*	324.2–343.2	324.2	1.19	-0.05	0.62	-0.01	3D-Ising
0.930	323.2–343.2	321.8	1.20	-0.04	0.65	0.02	3D-Ising

Case 2: T_s values estimated by assuming mean field model were used.

$x_{\text{FA-}d2}$	T range / K	$T_{\text{s mean field}}$ / K	γ	Difference from 1.00	ν	Difference from 0.50	Suitability
0.830	322.2–343.2	318.7	0.95	-0.05	0.53	0.03	*mean field*
0.876	324.2–343.2	324.3	1.03	0.03	0.54	0.04	
0.900*	324.2–343.2	324.5	1.03	0.03	0.54	0.04	
0.930	323.2–343.2	322.7	0.80	-0.20	0.45	-0.05	

*$x_{\text{FA-}d2}$ of the UCST composition.

Table S14 Critical exponents of γ and ν determined from fits on I_0 and ξ values of [C$_8$mim][TFSI]–FA-d_2 solutions at various $x_{\text{FA-}d2}$, respectively, with T_s estimated from the partial T range of Fig. S33–S36. Differences give the values between the estimated critical exponents and the typical ones of γ (1.24 and 1.00) and ν (0.63 and 0.50). Suitability refers to which model better explains the I_0 and ξ values when comparing the results of Cases 3 and 4. The description of the model's name indicates the better explanation.

Case 3: T_s values estimated by assuming 3D-Ising model were used.

$x_{\text{FA-}d2}$	T range / K	$T_{\text{s 3D-Ising}}$ / K	γ	Difference from 1.24	ν	Difference from 0.63	Suitability
0.830	322.2–333.2	317.2	1.15	-0.09	0.63	0.00	*3D-Ising*
0.876	324.2–333.2	323.5	1.18	-0.06	0.66	0.03	3D-Ising
0.900*	324.2–333.2	324.2	1.19	-0.05	0.61	-0.02	3D-Ising
0.930	323.2–343.2	321.9	1.16	-0.08	0.64	0.01	3D-Ising

Case 4: T_s values estimated by assuming mean field model were used.

$x_{\text{FA-}d2}$	T range / K	$T_{\text{s mean field}}$ / K	γ	Difference from 1.00	ν	Difference from 0.50	Suitability
0.830	322.2–333.2	319.0	0.89	-0.11	0.49	-0.01	
0.876	324.2–333.2	324.1	0.61	-0.39	0.35	-0.15	
0.900*	324.2–333.2	324.4	1.08	0.08	0.57	0.07	
0.930	323.2–333.2	322.7	0.77	-0.23	0.43	-0.07	

*$x_{\text{FA-}d2}$ of the UCST composition.

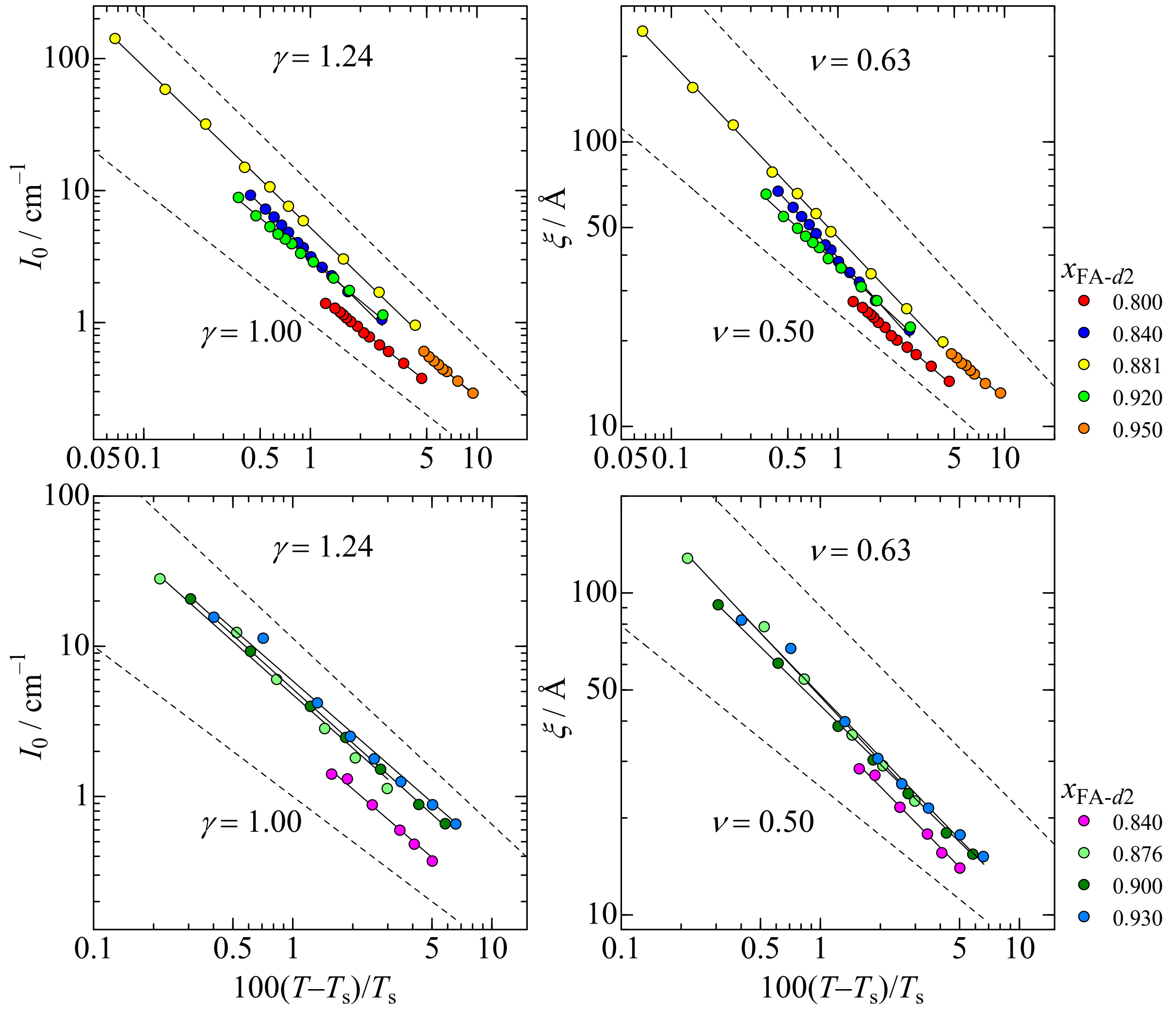

Fig. S37 γ and ν determined by fits for I_0 and ξ values of [C$_6$mim][TFSI]–FA-d_2 (top) and [C$_8$mim][TFSI]–FA-d_2 (bottom) solutions at various $x_{\text{FA-}d2}$. The dashed lines show the slopes of the typical γ (1.24 and 1.00, respectively) and ν (0.63 and 0.50, respectively) values for 3D-Ising and mean field.